Bulletin of the Seismological Society of America, Vol. 97, No. 2, pp. 357–378, April 2007, doi: 10.1785/0120060153

Ⓔ

Recovering Seismic Displacements through Combined Use of 1-Hz GPS and Strong-Motion Accelerometers

by Gordon L. Emore, Jennifer S. Haase, Kyuhong Choi, Kristine M. Larson, and Atsushi Yamagiwa

Abstract Retrieving displacement from seismic acceleration records is often difficult because unknown small baseline offsets in the acceleration time series will contaminate the doubly integrated record with large quadratic errors. One-hertz Global Positioning System (GPS) position estimates and collocated seismic data are available from the 2003 M_w 8 Tokachi-Oki (Hokkaido) earthquake. After a process of correcting for possible misorientation of the seismic sensors, an inversion method is used to simultaneously solve for ground displacement with both data sets as input constraints. This inversion method takes into account the presence of unknown offsets in the acceleration record, and the relatively large uncertainties in the estimated 1-Hz GPS positions.

In this study, 117 channels of seismic data were analyzed. Only 5% of the time does the static displacement retrieved from traditional baseline correction processing without GPS information agree with the absolute displacement measured with 1-Hz GPS to within the errors of the GPS data. In solving simultaneously for constrained displacements that agree with both the seismic and GPS data sets, an optimal solution was found that included only one- or two-step functions in the acceleration records. Potential explanations for the offsets are analyzed in terms of tilt of the sensor or electronic noise. For nine stations, clear misorientations of the seismic sensors of more than 20 deg from the reported orientation were found. For this size event, the 30-sec sampled GPS solutions were also a sufficient constraint for establishing the offset errors and recovering reliable displacements. The results significantly extend the frequency band over which accelerometer data are reliable for source inversion studies.

Online material: Plots of constrained seismograms with metadata.

Introduction

Seismic recordings are used to model the complexities of fault rupture by computing the response of the crust to displacements that occurred on the fault plane and fitting those to the observed seismograms (Hartzell and Heaton, 1983; Okada, 1985). Ideally this type of source inversion uses both teleseismic seismograms that provide a strong constraint on the total seismic moment with little sensitivity to uncertainties in crustal structure, and near-source strong-motion accelerometer records that provide higher resolution of the spatial location of slip on the fault (Wald and Heaton, 1994). The strong-motion records must be converted to displacement or velocity for the source inversion calculation. There are various sources of errors in the accelerometer records that are amplified when the acceleration is integrated. The three most commonly attributed sources include large-scale tectonic tilt, local tilt due to ground failure, and nonlinear behavior of the seismometer itself (Trifunac and Todorovska, 2001). To deal with these errors, the records are usually bandpass filtered from ~20 sec to 0.2 sec. Other static corrections may be made after qualitative evaluation of the characteristics of the recording to provide displacements that are constant after the event. Motivation to extend the low-frequency end of the usable range has been fueled by important advances in fault slip and rupture modeling and inverse problems to recover time histories of displacement on the causative fault (Hartzell and Heaton, 1983; Wald and Heaton, 1994; Ji *et al.*, 2004).

Seismic recordings from large earthquakes are also used to derive information about the levels of ground motion that structures should be designed to withstand. Depending on the properties of the structure, and in particular, the size, the response to a given ground motion may vary (Celebi, 2000).

For large structures, for example, buildings greater than 10 stories tall, the fundamental period of building response is typically greater than 1 sec, and so the design of these buildings depends on knowledge of these long-period ground motions. Some very tall buildings, for example, are sensitive to 10-sec periods and greater (Kramer, 1996). In addition, large buildings have been shown to temporarily lengthen their natural periods when subjected to shaking, independent of any structural damage that may be inflicted (Trifunac and Todorovska, 2001; Clinton, 2004). Active and semiactive control systems have been designed to reduce the response of large base-isolated structures to ground motion (Symans *et al.*, 1999). The control systems typically use hydraulics or magnetorheological dampers to adjust the rigidity of the structure with time during the earthquake shaking. Managing structural response is more difficult in the near field where large velocity pulses may be present in the seismic ground motions that can result in permanent deformation and large interstory drifts in the structures. Much of the recent work on new techniques in base isolation of large structures and active and passive damped systems rely on characteristics of the 1994 Northridge, the 1995 Kobe, and the 1999 Chi Chi Taiwan earthquakes, where near-field ground motions with large velocity pulses were observed (Spencer *et al.*, 2000). The work discussed here provides an additional dataset of strong ground motions whose accuracy in the 3 to 15-sec range crucial for tall buildings can be estimated quantitatively based on independent data.

The use of near-field strong ground motion accelerograms for both understanding the seismic source and for improving the response of buildings to strong shaking is subject to the correct interpretation of doubly integrated records that may have serious errors. These errors are typically hidden within the strong-shaking portion of an acceleration record, and are only visible once the record is integrated. The errors in the accelerograms are thought to be due to hysteresis in the sensor, problems in the analog-to-digital converter, and tilting or rotation of the ground (Boore *et al.*, 1980, 2002; Trifunac and Todorovska, 2001). Problems often occur because of changes in the base level of the acceleration record during or after violent shaking. Analysis of these errors may be complicated by recordings that begin after the first arrival or stop before shaking has stopped. These small offsets in the reference level of motion create large errors in the integrated record (Boore *et al.*, 2002). In addition, very small angles of ground tilt may lead to shifts in the baseline in both horizontal acceleration components. This may be due to actual tectonic tilt of a large-scale area, or to more localized ground failure during an earthquake (Clinton, 2004; Trifunac and Todorovska, 2001). The different sources may be separated to some degree by the predictability of their behavior. Tilt effects are restricted to the horizontal components for small angles of tilt, and are extremely sensitive. For example, a cumulative 5-cm error in displacement over 100 sec may be caused by a tilt of merely 1 microradian, if we use the relation

$$\theta_s = \frac{\Delta acc}{g}, \tag{1}$$

where θ_S is the local tilt, Δacc is the acceleration offset, and g is the acceleration of gravity. The tectonic tilt may be predicted by using regional Global Positioning System (GPS) stations to get the change in vertical displacement over distance

$$\theta_T = \frac{\Delta Z_A - \Delta Z_B}{L}, \tag{2}$$

where θ_T is the predicted tectonic tilt, ΔZ is the vertical displacement at two sites A and B, and L is the distance between A and B. If the offsets in the acceleration signal correspond reasonably well to the prediction, it may be assumed that they are due to the tectonic displacement over a large area. If they do not correspond well, they may be due to local-site ground failure or setting. If there are nonnegligible offsets in the vertical direction, then the offsets may not be easily ascribed to tilt at all, and may be related to nonlinearities within the seismometer itself (Clinton, 2004; Trifunac and Todorovska, 2001).

This article investigates the characteristics of the acceleration errors and the evaluation of methods to correct them, given that independent measurements of displacement are now available from 1-Hz GPS observations of the Tokachi-Oki earthquake. Given the importance of determining accurate seismic displacements as discussed earlier, the reviews the current methods for processing strong-motion signals, the Strong-Motion Data Processing section the Data from the Tokachi-Oki Earthquake section introduces comparisons between 1-Hz GPS and seismic data for the 2003 Tokachi-Oki earthquake, and the 1-Hz GPS Measurements section describes the techniques for retrieving 1-Hz GPS displacement estimates. The Comparisons between Seismic and 1-Hz GPS Data section discusses the nature of some of the errors in the seismic-acceleration records, the sixth section introduces the techniques developed to combine 1-Hz GPS and seismic data to retrieve more accurate near-source displacements, and the Comparison of Constrained Solution to Alternative Approaches section summarizes the results and discusses the frequency of occurrence and magnitude of typical strong-motion reconstruction errors.

Strong-Motion Data Processing

Historically, reliable estimates of the peak ground acceleration and the acceleration response spectra have been the primary products of strong-motion monitoring. With advances in digital sensor technology, however (digital, higher dynamic range sensors with longer pre-event and postevent buffers), there is great interest in extending the usable frequency band to lower frequencies. In the typical uses of the data, the frequencies of interest are at about 1 Hz, and the objective of strong-motion data processing is to estimate

those products from the usable frequency band of the record and filter out low-frequency noise (Shakal *et al.*, 2004). The noise spectrum increases linearly as period increases, so criteria have been defined for the low-frequency cutoff, such as where the signal-to-noise drops below a factor of 2–3 (Trifunac, 1977; Trifunac and Lee, 1978). Similar processing systems are in use by the California Strong Motion Instrument Program (CSMIP) (Shakal *et al.*, 2005), the National Strong Motion Program (NSMP) (Converse and Brady, 1992; Stephens and Boore, 2004), and the Pacific Earthquake Engineering Research Center (PEER) (Abrahamson and Silva, 1997; Darragh *et al.*, 2004) in the United States, and the Taiwan Strong Motion Instrumentation Program (TSMIP) array (Loh, 2004).

The basic method, as implemented in NSMP processing (Converse and Brady, 1992), uses high-pass (0.02 Hz) and low-pass (50 Hz) Butterworth filters. After removing the mean, tapering, and removing the instrument response, the filter corner frequencies are adjusted by reviewing the initial estimates of the spectra. The velocity and displacement are computed by time-domain integration. Then the acceleration, velocity, and displacement are plotted and reviewed visually.

Techniques for correcting acceleration baseline errors to retrieve lower-frequency information and static offsets typically fit a slope to the velocity trace and then subtract the derivative of this correction signal from the original accelerometer record before a final integration to velocity or displacement (Boore, 2001; Boore *et al.*, 2002). With this method, a displacement record is recovered that is constant after strong ground shaking has ended, though it is a very subjective process. It has been suggested that although a zero postevent velocity is a condition for a baseline-corrected signal, it may not be well enough constrained to recover an accurate coseismic displacement (Boore and Bommer, 2005). In the absence of GPS data, stability of the correction technique and general agreement in final offsets among nearby sites are criteria that are used to judge the reliability of the baseline corrections.

The procedure of baseline correction to preserve static permanent or tectonic displacements in near-source recordings (<20 km from the fault), as implemented in the PEER database processing is as follows:

1. Make a least-squares fit to the integrated acceleration (velocity records) using three functional forms: linear fit to velocity, bilinear piecewise continuous fit, and a quadratic fit to velocity.
2. Make a systematic search of the start time of the fitting function to determine the best-fitting functional form.
3. Differentiate the best-fitting function and then remove it from the original acceleration trace.
4. Low-pass filter with a causal Butterworth four-pole filter with corner near 50 Hz to remove high-frequency noise.
5. Time integrate acceleration trace to produce velocity and displacement time histories.
6. Plot acceleration, velocity, and displacement and review visually.

A detailed review of this technique to retrieve absolute displacements applied to the 1999 Hector Mines earthquake and the 1999 Chi-Chi, Taiwan, earthquake demonstrates results that appear to be consistent with the previously mentioned criteria: zero postevent velocity and constant static displacement, stability in the correction algorithm, and final offset consistency among nearby sites (Boore, 2001; Boore *et al.*, 2002). However, no independent means exist for verifying the final displacements. Total displacement results from both earthquakes have been compared with static displacements retrieved from static GPS measurements processed for a daily average position. These presume that the entire static displacement occurred during the earthquake with no postseismic deformation during the averaging period following the event. The seismic-displacement time series derived from the acceleration cannot be verified during and immediately after the shaking with the static GPS result alone. In the sections that follow, we apply the strong ground motion processing procedure described previously to the data from the 2003 Tokachi-Oki (Hokkaido) earthquake, and compare the results with the GPS displacement time series to formally estimate the uncertainties involved with retrieving absolute displacement.

Data from the Tokachi-Oki Earthquake

The 25 September 2003 Tokachi-Oki earthquake occurred at 19:50:07 UTC. The epicenter was located ~80 km southwest of the Hokkaido coast of Japan, close to the location of the 1952 Tokachi-Oki earthquake. Figure 1 shows the location of the epicenter with respect to the Japanese islands. The earthquake had moment magnitude estimated at M_w 8.0 (Honda *et al.*, 2004). The earthquake occurred in the Kurile trench, on the boundary of the Pacific plate that is subducting beneath a sliver of the North American plate trapped between the Pacific plate and the Eurasian plate (Yamanaka and Kikuchi, 2003). The event generated shaking with one record showing levels as high as 1 *g* (at K-net station HKD100) and widespread areas of shaking greater than 0.2 *g* at stations close to the coast in eastern Hokkaido (Aoi *et al.*, 2004; Honda *et al.*, 2004). Coseismic deformation exceeded 1 m at some locations (Miura *et al.*, 2004). Table 1 summarizes the source parameters of the earthquake rupture (Yagi, 2004).

Seismic activity in Hokkaido is monitored by the National Research Institute for Earth Science and Disaster Prevention (NIED) with a seismic network composed of 75 broadband monitoring stations (Fnet), 185 strong-motion instruments (Knet), and 112 dual borehole/surface digital strong-motion seismometers (KiKnet) on the island of Hokkaido alone (Kinoshita, 1998; Aoi *et al.*, 2000, 2004; Okada *et al.*, 2004). The Knet instruments are 100-Hz K-NET95 strong-motion accelerometers. The KiKnet instruments are

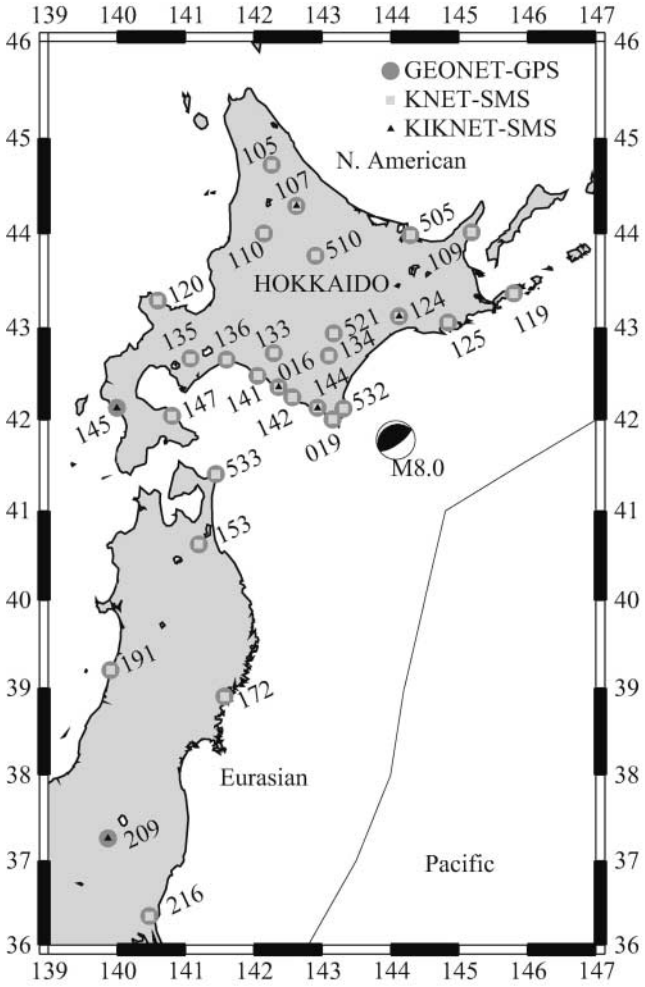

Figure 1. Locations are shown of 29 GEONET GPS stations in Japan that have either a Knet or KiKnet strong-motion station located within 4 km. The focal mechanism shows the location of the *M* 8 Hokkaido thrust earthquake. Numbers are the GEONET site identification code.

Table 1
Characteristics of the 2003 Tokachi-Oki Earthquake (Yagi, 2004)

Parameters	
Magnitude M_W	8.0
Latitude	1.78° N
Longitude	144.08° E
Depth	25 km
Strike	250°
Dip	20°
Rake	130°

200-Hz strong-motion accelerometers. For this study, 27 Knet and 6 dual-instrument surface/borehole KiKnet stations were used, chosen for their proximity to 1-Hz GPS sites as described subsequently.

A dense network of more than 1000 permanent GPS stations continuously records data for measuring surface deformation to support earthquake research in Japan (GEONET) (Miyazaki *et al.*, 1997; Yamagiwa *et al.*, 2006). Typically these data are available at a 30-sec sampling rate, which is sufficient for relative positioning of the site markers with an uncertainty on the order of millimeters, with the greatest precision on the horizontal components, over a daily solution period. Results from the network data from the Hokkaido earthquake show that coseismic displacements were as large as 1 m at 80 km from the epicenter (Miura *et al.*, 2004). The network also supports real-time differential GPS surveying and navigation, so 1-Hz data were available during times when the real-time transmission system was operational. In some cases, communications were lost during the earthquake for this system and high-rate GPS data were recovered for only a portion of the signal. In this article, 1-sec time series are used from 29 GEONET GPS sites on Hokkaido, located close to Knet and/or KiKnet digital strong-motion stations. The 1-Hz time series were augmented with 30-sec data at four sites, primarily to serve as an extra constraint for those sites with gaps in the 1-Hz signal due to communications outages. As shown in Figure 1, these collocated sites primarily lie along the southern and eastern coast, with a few scattered inland. Including all possible pairs of GPS and downhole or surface seismometers, there are a total of 39 site pairs collocated within 4 km.

Different attempts to model the earthquake fault motion have resulted in varying reconstructions of that motion. Comparisons of results for the 2003 Tokachi-Oki earthquake have shown different numbers of asperities, and 20-km differences in the location of maximum slip. These other results include published slip models using 25 teleseismic records (Yamanaka and Kikuchi, 2003), an inversion using 12 teleseismic stations and 12 surface strong-motion sites (Yagi, 2004), a model with 15 surface strong-motion sites (Honda *et al.*, 2004), and one using 11 borehole strong-motion sites and 70 GPS stations (Koketsu *et al.*, 2003). In addition, estimates of total fault slip were computed from static GPS measurements (Miura *et al.*, 2004). One of the conclusions was that, given the differences in frequencies sampled, sensitivities, and geometries of the observing networks, no one kind of instrument will provide all the information needed for finite-fault rupture studies. The results from this study should aid in such fault-slip inversions by providing absolute broadband displacements constrained by both strong ground motion and GPS recordings.

1-Hz GPS Measurements

The Global Positioning System is a constellation of satellites used to determine meter-level positions in real time. It is primarily used for navigation. The geodetic community has also developed methods for mm-level positioning in non-real-time (Segall and Davis, 1997). To achieve this precision, geodetic software must accurately model the orbital parameters of the satellites, account for atmospheric delays, and

solve for clock drifts and cycle ambiguities. In general, geodetic users estimate positions over long periods, ~24 hours. This allows static displacements of a site due to an earthquake to be computed, where an entire day or multiple days of GPS data are processed to retrieve a single average position before the earthquake and a single average position after the earthquake.

For 1-Hz GPS applications (Larson *et al.*, 2003), positions are estimated every second rather than averaged. In this study, positions are estimated using the GIPSY software (Lichten and Border, 1987) with orbits held fixed to precise IGS values (Beutler *et al.*, 1994). Positions are defined in the ITRF2000 reference frame (Altamimi *et al.*, 2002). Reference sites were chosen to be more than 400 km from the source region to avoid any contamination by strong ground motion at the reference sites, as was seen in Irwan *et al.* (2004). The method is described in more detail in the electronic supplements for Larson *et al.* (2003) and Miyazaki *et al.* (2004a). For this dataset, short-term precision has been evaluated as 4, 7, and 15 mm for the east, north, and vertical components (Miyazaki *et al.*, 2004a). Thirty-second GPS records were also analyzed for some of the sites with communications outages. It needs to be emphasized that all of these receivers operated at 1 Hz, but in some cases only every 30th value was saved in memory. So, in principle, the 30-sec values should agree exactly with the coincident 1-Hz records.

Comparisons between Seismic and 1-Hz GPS Data

In this section we evaluate the accuracy of the long-period components of the integrated strong-motion seismic displacements through comparison with 1-Hz GPS time series. For the purposes of much of the first portion of the study dealing with sensor orientation, both the strong-motion acceleration and GPS displacement signals were high-pass filtered at 30-sec periods to remove the static offset. Long-period comparisons will be examined later in this section. We did not remove an instrument response from the accelerometer records, because we assumed the instruments had a flat response to acceleration within the frequency range of interest.

Theoretically a filtered, integrated strong-motion displacement history should match well with a filtered displacement record taken from a nearby 1-Hz GPS sensor. Some differences may be expected because of the distance separating the collocated instruments, so the effect of the separation was investigated to determine how close the GPS and strong-motion sites need to be to each other to be considered collocated.

During this investigation, it was found that the horizontal orientations of some sensors were not well documented and were in fact rotated a significant amount from the assumed northeast orientation, as noted previously (Clinton, 2004; Miyazaki *et al.*, 2004a). A misalignment of the seismometer could very easily produce significant differences between the seismic and GPS records. To test this, a comparison was made between the integrated strong-motion data and the 1-Hz GPS records at 26 sites where strong-motion and GPS sensors were located within 1.6 km of each other, which is the dominant wavelength of the seismic energy. Some small separation between the sensors was deemed acceptable because the long-period waveforms for large earthquakes usually change little over small distances if the local topography and geology remain similar (Boore *et al.*, 2002). The comparison was extended to 39 pairs to examine any possible decrease in correlation for separations up to 4 km. Seventy-seven pairs of sites with separations up to 20 km were compared to test the extreme limit where intercomparisons could be made.

In Figure 2a and b, the 100-Hz Knet station HKD110 (decimated to 10 Hz) is shown with the 1-Hz GEONET GPS station 950144 and in Figure 2c and d, the 200-Hz KiKnet station HDKH07 (decimated to 10 Hz) is shown also with GPS station 950144. For this comparison, all these signals are high-pass filtered at a 30-sec period to remove the static offset. These site pairs are considered effectively collocated because they are within 1.6 km of each other. The north component for site HKD110 shows a significant difference between the time-aligned strong-motion signals and their counterpart GPS records, whereas the agreement with site HDKH07 is much better. However, as the figures also show, an imposed rotation of the two horizontal components of the strong-motion signal at HKD110 allows the signals to match a great deal better. This would imply that the sensor misorientations for at least a few of the sites examined were not reported. Although most sites required either no or small rotation angles, several required significant rotations to the time series to remain consistent (Table 2). One such site, KiKnet KKWH05, was apparently rotated by almost 90 deg.

A grid-search approach was used to compare high-pass-filtered GPS signals with their high-pass-filtered strong-motion counterparts over a range of possible rotation angles. An example of this is shown in Figure 3, where the record from GEONET GPS station 950144 is compared with the integrated displacement from Knet station HKD110. The root-mean-squared error between the two signals shows a definite minimum as the strong-motion horizontal displacement components are subjected to a series of rotations. In this case the strong-motion sensor was off by 40 deg with an uncertainty of ± 28 deg. The National Research Institute for Earth Science and Disaster Prevention (NIED) in Japan is aware of the possible misorientation of some of the older Knet seismometers and provides this information to researchers when it becomes available (J. F. Clinton, personal comm., 2006; K. Irikura, personal comm., 2006). Orientation estimates from this study will be submitted to NIED.

With these sensor rotations taken into account, it becomes possible to examine the effect of separation when comparing records from strong-motion and GPS sites that are close but not exactly collocated. The limitation in the level of agreement that is expected between two sites due to

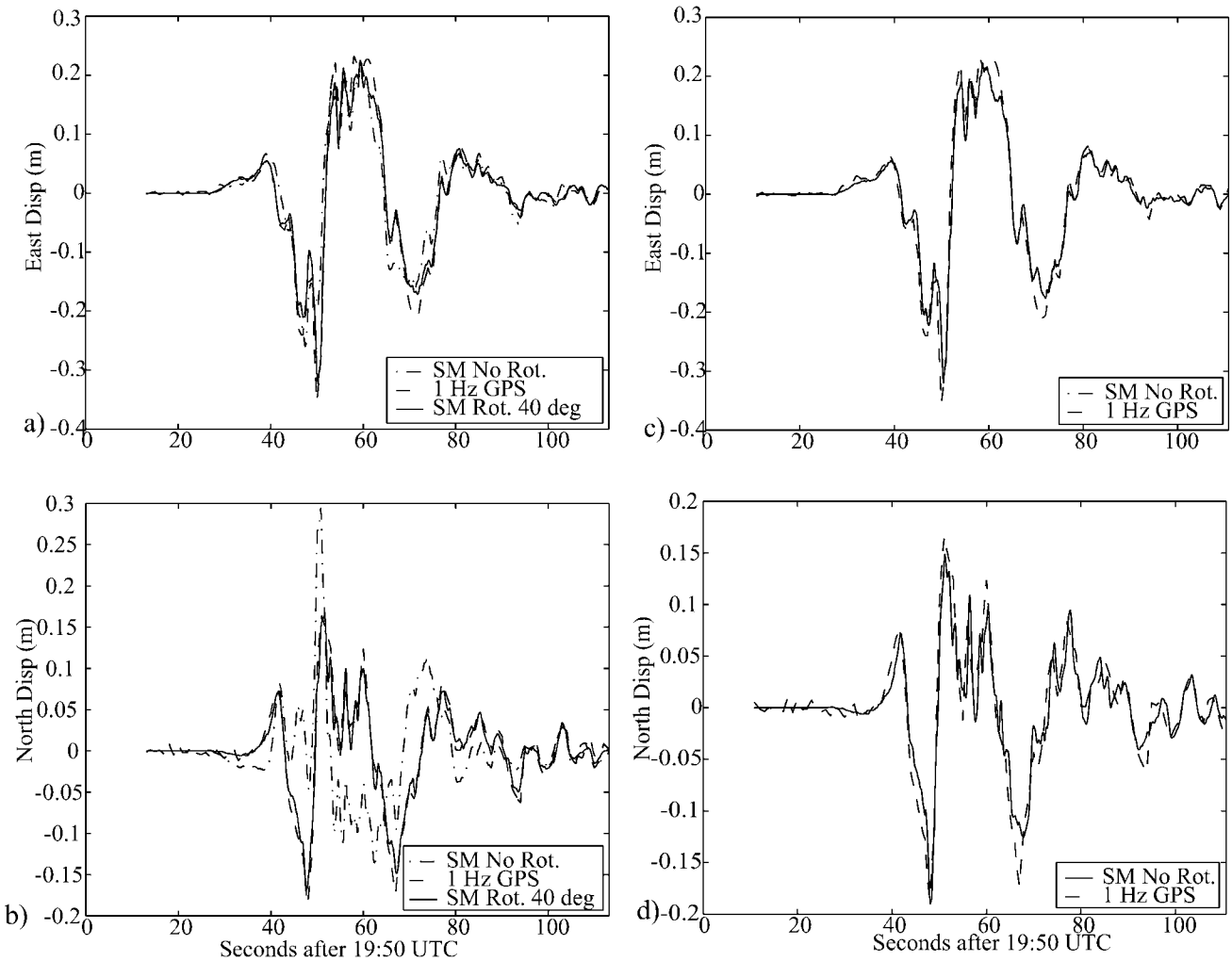

Figure 2. High-pass-filtered displacement seismograms are shown for the east component (a) and the north component (b) of Knet site HKD110 and GEONET 950144 and the east component (c) and the north component (d) of KiKnet site HDKH07 and GEONET 950144. Strong-motion records were time shifted to account for small site separations. Strong-motion displacements (dot-dashed lines) agree well with GPS displacements (dashed lines) for HKDH07, but not for HKD110. Rotating HKD110 by 40 deg (solid line) agrees much better with the GPS.

varying site conditions was quantified in the following manner. The standard deviation of the difference between the GPS and integrated strong-motion signals normalized by the maximum amplitude of the filtered GPS signal is used as an error measure for the agreement between these filtered signals. This normalized standard deviation is described as:

$$Err = \frac{\sum_{j=1}^{2}\sum_{i=1}^{nt}(u_{\mathrm{SM}i,j} - u_{\mathrm{GPS}i,j})}{(2 \cdot nt - 1) \cdot \max(u_{\mathrm{GPS}i,j})}, \qquad (3)$$

in which $u_{\mathrm{SM}i,j}$ is the filtered doubly integrated strong-motion time series (decimated to 10 Hz) for component j, $u_{\mathrm{GPS}i,j}$ is the filtered zero mean 1-Hz GPS displacements (resampled at 10 Hz) for component j, and nt is the number of time samples. The strong-motion time series was shifted in time by an amount proportional to the difference in epicentral distance.

This metric for goodness of fit was chosen because it is insensitive to the overall magnitude of the signal. As Figure 4a illustrates for sites where no orientation error was present, when the strong-motion and GPS signals are time aligned to account for different distances to the earthquake hypocenter, there was no strong trend in the error with separation distance. This is also true for the other sites after the rotation errors are taken into account (Fig. 4b). The difference between the filtered GPS and the filtered strong-motion displacements for a large earthquake with the signal energy dominated by coherent lower frequencies is small for sites with a relatively wide separation, up to 15 km (Fig. 4c). This was observed for the 1999 Hector Mine earthquake (Boore *et al.*, 2002).

Table 2
A Summary of 39 GPS–Strong-Motion Site Pairs Examined in This Study, with Orientation Errors

GPS	Strong Motion	Strong-Motion Network	GPS Latitude (°)	GPS Longitude (°)	K_m Sep.	K_m Range	Orientation Error (deg)	Uncertainty in Angle	Normal S.D. Error in Filtered Rotated Signal (m/m)	Normal S.D. Error in Filtered Unrotated Signal (m/m)
940016	HKD106	Knet	42.4	142.4	2.1	154.9	9	22	0.009	0.009
940016	HDKH06	KiKnet +	42.4	142.4	1.1	154.9	−9	20	0.053	0.061
940016	HDKH06	KiKnet −	42.4	142.4	1.1	154.9	1	17.5	0.058	0.058
940019	HKD111	Knet	42.0	143.2	1.0	80.3	22	23.5	0.031	0.083
950105	HKD026	Knet	44.7	142.3	0.3	357.8	52	8	0.076	0.262
950107	HKD029	Knet	44.3	142.6	2.3	302.6	15	26	0.069	0.091
950107	KKWH05	KiKnet +	44.3	142.6	0.9	302.6	0	21.5	0.045	0.045
950107	KKWH05	KiKnet −	44.3	142.6	0.9	302.6	−85	22	0.045	0.26
950109	HKD064	Knet	44.0	145.2	0.6	264.2	22	*	0.127	0.132
950110	HKD115	Knet	44.0	142.2	0.2	291.7	26	8	0.073	0.159
950119	HKD074	Knet	43.4	145.8	0.5	224.7	−4	14.5	0.073	0.074
950120	HKD138	Knet	43.3	140.6	0.7	328.3	9	10	0.067	0.084
950124	HKD084	Knet	43.1	144.1	1.0	149.1	8	34	0.041	0.045
950124	KSRH02	KiKnet +	43.1	144.1	1.0	149.1	0	34.5	0.039	0.039
950124	KSRH02	KiKnet −	43.1	144.1	1.0	149.1	0	32.5	0.04	0.04
950125	HKD076	Knet	43.1	144.8	1.4	155	14	27	0.053	0.064
950133	HKD103	Knet	42.7	142.3	0.5	179.8	1	25.5	0.033	0.033
950134	HKD096	Knet	42.7	143.1	3.0	129.7	2	19	0.051	0.052
950135	HKD134	Knet	42.7	141.1	0.6	264.8	37	16.5	0.05	0.16
950136	HKD129	Knet	42.7	141.6	2.7	224.8	2	20	0.08	0.08
950141	HKD105	Knet	42.5	142.1	0.2	183.1	39	49.5	0.027	0.07
950142	HKD108	Knet	42.2	142.6	0.3	134.9	38	22.5	0.036	0.134
950144	HKD110	Knet	42.1	142.9	0.4	102.1	40	27.5	0.033	0.117
950144	HDKH07	KiKnet +	42.1	142.9	1.3	102.1	−1	24	0.044	0.044
950144	HDKH07	KiKnet −	42.1	142.9	1.3	102.1	0	22.5	0.046	0.046
950145	HYMH03	KiKnet +	42.1	140.0	0.3	338.4	10	16	0.057	0.071
950145	HYMH03	KiKnet −	42.1	140.0	0.3	338.4	−3	15.5	0.059	0.061
950147	HKD155	Knet	42.0	140.8	0.4	272	20	10.5	0.069	0.118
950153	AOM021	Knet	40.6	141.2	1.8	275.1	−13	*	0.18	0.188
950172	MYG001	Knet	38.9	141.6	0.5	386.6	−6	*	0.157	0.16
950191	AKT020	Knet	39.2	139.9	0.8	459.5	−1	*	0.157	0.133
950209	FKSH05	KiKnet +	37.3	139.9	1.2	625.5	−7	*	0.172	0.127
950209	FKSH05	KiKnet −	37.3	139.9	1.2	625.5	3	*	0.185	0.185
950216	IBR006	Knet	36.3	140.5	3.0	685.2	−58	*	0.226	0.361
960505	HKD058	Knet	44.0	144.3	3.5	246.2	1	*	0.093	0.093
960510	HKD035	Knet	43.8	142.9	0.5	240.8	15	11.5	0.054	0.103
960521	HKD095	Knet	42.9	143.2	4.0	148.6	11	*	0.094	0.096
960532	HKD113	Knet	42.1	143.3	0.3	73.8	22	10.5	0.066	0.131
960533	AOM004	Knet	41.4	141.4	0.4	223.5	10	10	0.075	0.087

KiKnet sites are labeled with a + or − to denote surface or borehole instruments, respectively.

* indicates cases where no rotation angle would bring the seismograms into an acceptable level of agreement. Sites where the rotation angle was greater than 10 deg were rotated prior to the rest of the data analysis. Angles are defined as degrees north from east.

The higher-frequency differences in the nature of the waveform due to the separation of the sites can be treated as random noise that is the same order of magnitude as GPS observation error, as illustrated by the smallest error achievable at very close sites. This means that as long as the time offsets for site pairs are taken into account, strong-motion signals from an event of this scale may be compared usefully with GPS records within a larger radius than expected—on the order of 15 km. Much closer agreement is seen between the seismic and GPS records than was seen in Irwan *et al.* (2004), where contamination due to ground motion at the reference GPS site produced noise in their GPS displacements. The error level for the most closely collocated site pairs provides a threshold beyond which the error might be considered due to local site effects and environmental conditions. This error level evaluated for the horizontal components represents the limit of our ability to discern an optimal fit and is used as a criterion for establishing the error in the orientation angle. The error level is evaluated for three components for further comparisons of integration methodology.

An error limit of 0.09 contains two standard deviations of the lognormal distribution of the cases (Fig. 4d). A summary of the orientation errors for the set of 39 site pairs is

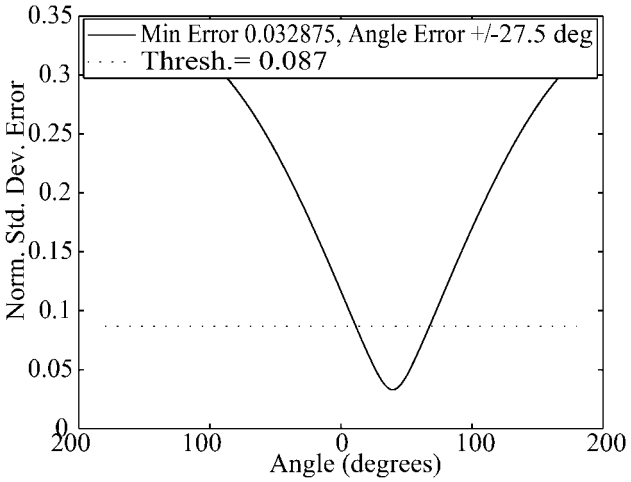

Figure 3. Normalized errors between GPS site 950144 and strong-motion site HKD110 filtered displacements as a function of rotation angle. There is a clear minimum at a 40-deg misorientation for the strong-motion sensor. The error threshold is shown by a dashed line and is described further in Figure 4. This threshold determines the uncertainty in the estimate of the rotation angle of ±27.5 deg.

presented in Table 2. As Figure 3 illustrates, this threshold applied to the error curve produces a range of orientations that result in acceptable levels of error, and therefore the error in the orientation angle, which is usually 10 to 20 deg. Site pairs with misfit levels above the threshold are indicated in the table with an *, even though in some cases there was a definite minimum in the error curve indicating a misorientation was likely. For sites where the misorientation was found to be greater than 10 deg, the GPS records were rotated by that angle before further analysis. Although it is technically the strong-motion records that should be rotated, rotation of the GPS data into the strong-motion orientation avoided mixing the contribution of long-period noise for different components during the determination of combined displacements. Once this was complete, all results were rotated to east, north, and up for consistency.

Combining GPS and Seismic Data to Retrieve Optimal Near-Source Displacements

With the availability of 1-Hz GPS displacements with accuracies within 4 and 15 mm, the possibility now exists of constraining the long-period instability during integration of accelerometer records and correcting for an any unpredictable offsets present within them that may be approximated as step functions. An inverse problem is constructed to solve for both the ground displacements at the seismic sensor, as well as a record of any offsets (noise) in the acceleration record. A discrete acceleration time history can be related to displacements via a central difference differentiation operator of the form:

$$
{}^{1}\!/_{dt^2}\begin{bmatrix} 1 & -2 & 1 & \cdots & 0 & 0 & 0 \\ 0 & 1 & -2 & \cdots & 0 & 0 & 0 \\ \vdots & \vdots & \vdots & \ddots & \vdots & \vdots & \vdots \\ 0 & 0 & 0 & \cdots & -2 & 1 & 0 \\ 0 & 0 & 0 & \cdots & 1 & -2 & 1 \end{bmatrix}\begin{bmatrix} u_1 \\ u_2 \\ u_3 \\ \vdots \\ u_{n-2} \\ u_{n-1} \\ u_n \end{bmatrix} = \begin{bmatrix} a_2 \\ a_3 \\ \vdots \\ a_{n-2} \\ a_{n-1} \end{bmatrix} \tag{4}
$$

$$
\equiv [D^2][\overline{u}_{\text{ground}}] = [\overline{a}_{\text{ground}}]
$$

where u_i is a displacement time series at time i, a_i is the corresponding acceleration time series, and dt is the sample interval of the two discrete signals. Additional constraints are added using collocated GPS measurements. The inverse problem is of the form:

$$
\begin{aligned} &\text{forward} : A\overline{u}_{\text{ground}} = \overline{d} \\ &[A][\overline{u}_{\text{ground}}] = \begin{bmatrix} \overline{a}_{\text{SM}} \\ \overline{u}_{\text{GPS}} \end{bmatrix} \\ &\text{inverse} : \overline{u}_{\text{ground}} = A_g^{-1}\overline{d}. \end{aligned} \tag{5}
$$

where d represents the data vector, containing both the strong-motion (SM) acceleration time series and any available collocated GPS displacement time series. The matrix A is the operator for the system, containing both differentiators and identity matrices. u_{ground} is the unknown vector of actual ground displacements. A_g^{-1} is the generalized inverse of A including the covariance matrix. The unknown accelerometer offsets, $n_{\text{noiseparameters}}$, are introduced as a series of step functions that can occur at any time during the time series. This modifies the inverse problem to be:

$$
\begin{bmatrix} \overline{a}_{\text{SM}}^{\text{10Hz}} \\ \overline{u}_{\text{GPS}}^{\text{1Hz}} \\ \overline{u}_{\text{GPS}}^{\text{30sec}} \end{bmatrix} = \begin{bmatrix} [D^2] & [H] \\ [I^{\text{10Hz}\rightarrow\text{1Hz}}] & [0] \\ [I^{\text{10Hz}\rightarrow\text{30sec}}] & [0] \end{bmatrix}\begin{bmatrix} \overline{u}_{\text{ground}}^{\text{10Hz}} \\ \overline{n}_{\text{noiseparameters}} \end{bmatrix} \tag{6}
$$

$$
A_g^{-1} = [A^T C_d^{-1} A]^{-1} A^T C_d^{-1} \tag{7}
$$

$$
[C_d^{-1}] = \begin{bmatrix} \left[1/\sigma_{\text{SM}}^2\right] & [0] & [0] \\ [0] & \left[1/\sigma_{\text{1HzGPS}}^2\right] & [0] \\ [0] & [0] & \left[1/\sigma_{\text{30secGPS}}^2\right] \end{bmatrix} \tag{8}
$$

in which D^2 is the central difference operator, I is a reduced identity matrix that selectively samples the displacement vector at 1 sec or 30 sec to correspond with the GPS sam-

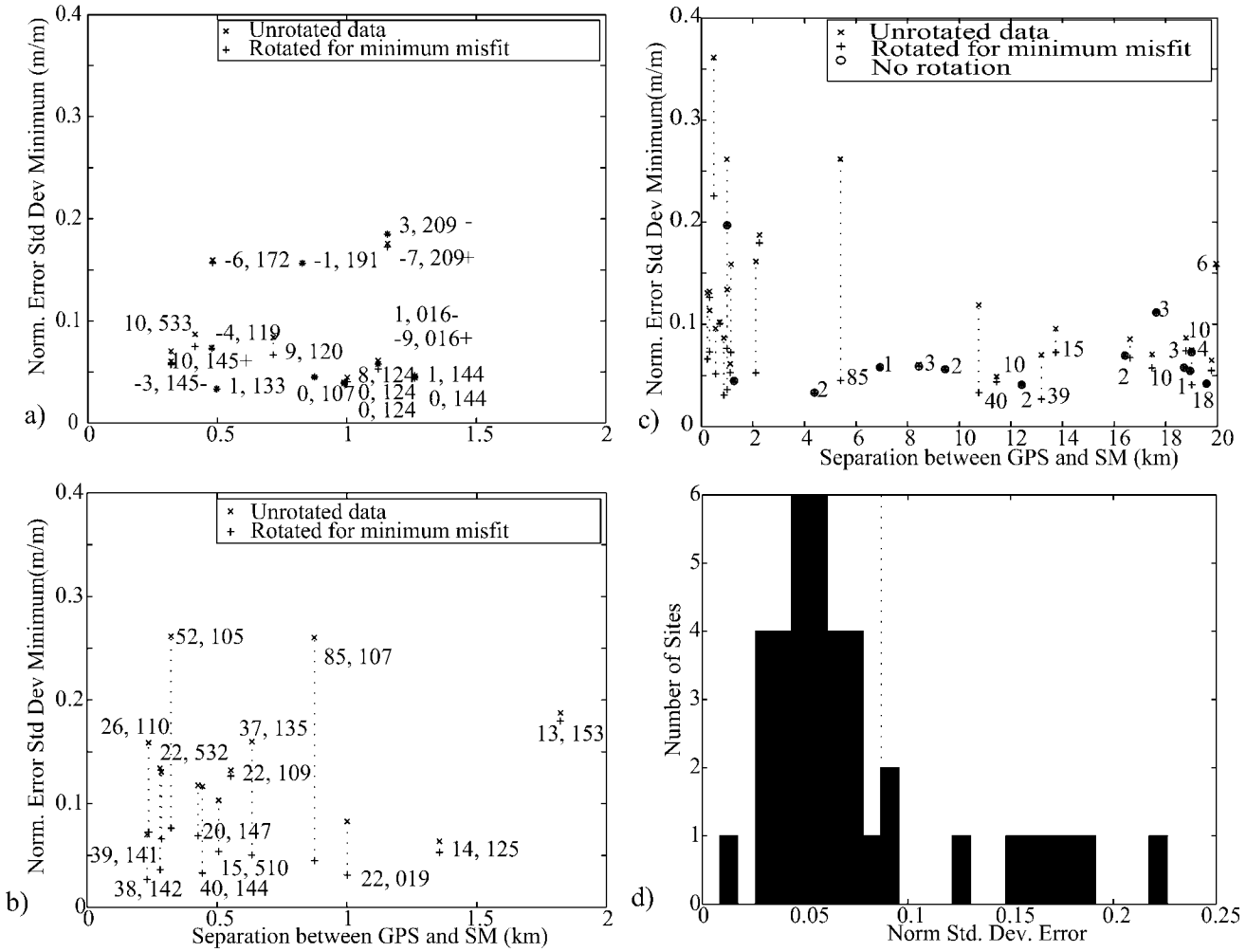

Figure 4. (a) Normalized error between filtered GPS and time-aligned, rotated, and filtered integrated strong-motion records as a function of site separation up to 2 km for sites where no significant orientation error is present. The first number next to the symbol is the rotation angle and the second number is the last 3 digits of the GPS site ID, with + or − indicating Kiknet surface or borehole sensor. (b) Normalized error for sites with orientation errors. × indicates misfit level for the unrotated data, and + indicates the misfit for the same site after rotation to the minimum error level. (c) Normalized error for all site pairs with site separations up to 20 km. After time shifting the seismograms to account for different propagation distances, the data agree at a comparable level for separations up to 15 km. (d) Histogram of normalized error for all sites after rotations. Two standard deviations of this lognormal distribution yields a criterion of 0.09 as the threshold of misfit. This threshold of 0.09 is used to determine the rotation angle error in Figure 3.

pling, operator H contains the Heaviside functions that map step function offsets at fixed times, and C_d^{-1} is a weighting matrix, based on the uncertainties in the data. Estimates for the uncertainties in the GPS data processing lead to a value of 4 mm for the east component GPS record, 7 mm for the north component, and 15 mm for the vertical component (Miyazaki *et al.*, 2004a). The goal is to fit the data such that the agreement between the GPS and strong motion is within the threshold value of the 0.09 level determined earlier. The seismic data are weighted by the Knet digitization precision of 0.015 cm/sec^2, which weights the seismic data more heavily than the GPS data as justified by the higher precision, to maintain the higher-frequency character of the desired signal. Because 1-Hz GPS data are not always available, we have constrained portions of the seismic signal for a few sites using 30-sec GPS data.

In the first phase of processing, the accelerometer data are decimated from 100 to 200 Hz to produce a 10-Hz time series. The point of combining the strong-motion data with the GPS data is to retain the higher frequency character of the accelerometer data while gaining the low-frequency displacement behavior of the GPS data. Frequencies above

10 Hz, being outside the frequency range of interest, are removed to reduce the time and memory requirements for the least-squares procedures. A standard integrated strong-motion displacement signal may be seen in Figure 5, compared with the nearby GPS station. Notice the severe effect of extremely small acceleration shifts when the signal is integrated, producing a parabolic trend in displacement and a slope in velocity.

The next phase is to correct for site rotations. The GPS displacement is rotated by the angle found from the minimization process described in the previous section, given in Table 2.

For comparison purposes, the strong-motion signal is baseline corrected using a procedure similar to the methodology employed for the PEER database (Boore, 2001). The baseline correction removes the trend present in the velocity trace. The baseline-corrected seismograms show good agreement with GPS results early in the event history (Fig. 5). The correction removes the obvious parabolic baseline error for the north–south component and produces a time series where the velocity is zero and displacement is constant after the shaking has stopped. Unfortunately, because of the nature of integration, very small deviations in the velocity signal from a linear baseline can produce a large discrepancy in the displacement record. The acceleration record in this particular case is reasonably well behaved, but still produces some erroneous offsets of as much as 20 cm. These signals are calculated for comparison only and are not used further in the constrained integration scheme.

Finally, the actual combined displacement solution is calculated as described in the inverse problem, using the unfiltered accelerometer records, using a simple step function model to represent the unknown acceleration offsets, and utilizing 1-sec and 30-sec GPS data to constrain the signal. Although it might be expected that a step function offset that was due to an instantaneous tilt of the three-component sensor would produce significant offsets on the two horizontal components at the same time, each component was computed separately. In this way the hypothesis of local ground tilt as the cause of offsets could be tested. Because the timing of the Heaviside step functions is unknown, an iterative search method is used where the starting time of the step function is assumed and the inverse problem is solved. The start time of the step is changed and the process is repeated. The minimum misfit solution is selected. If a single step function does not satisfy the misfit criterion of 0.09, then a second step function is added and the iterative process is repeated for the second step function. If the two step function solution has a misfit less than 0.09 or has a misfit reduction of more than 50% over the single step function solution, then it is kept as the optimal solution. Otherwise the single step function solution is retained. An example showing the result of the constrained inversion is shown in Figure 6. The combined displacement removes the estimation noise of the GPS data and replaces it with a more precise integrated displacement at that frequency. The combined displacement is smoother than the 1-Hz GPS, but has a reliable coseismic offset. These combined displacement seismograms are presented in Figure 7 for all site pairs, and the corresponding velocity and acceleration seismograms for a few selected sites are included in Figures 8 and 9. Ⓔ A complete set of seismograms is included in the electronic edition of BSSA. Displacements can be retrieved with confidence as far as 460 km from the epicenter even though they are quite small.

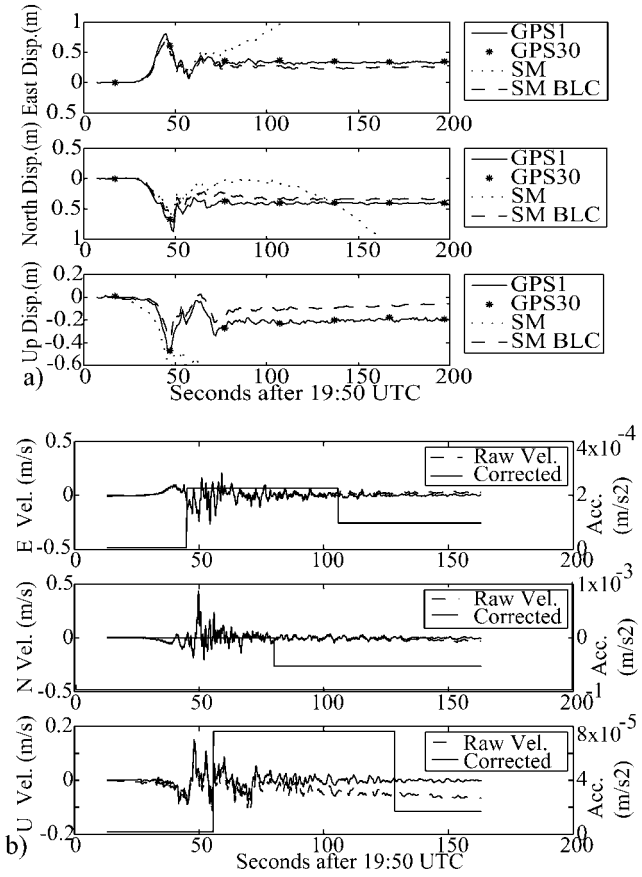

Figure 5. (a) 1-Hz GPS displacement for site 950144 (solid line), GPS 30-sec solution for displacement (stars), uncorrected integrated strong motion for Knet site HKD110 (dotted line), and baseline-corrected integrated strong-motion record (dashed line). (b) Velocity seismograms for the same site before baseline correction (dashed line) and after correction (solid line). The timing of the step functions applied during the baseline correction is shown for reference. Note the change in scale and trend in raw velocity for the vertical component.

There is a possibility that the ground motion contains a significant component of time varying tilt (Grazier, 2004). To explore this possibility, we perform a test where we specify in advance the starting time of a large number of step functions (10, for example) and solve the inverse problem. With a generalized inverse and weak constraint on the size of the step functions, this ill-constrained problem can be solved. We found that this approach usually produces one

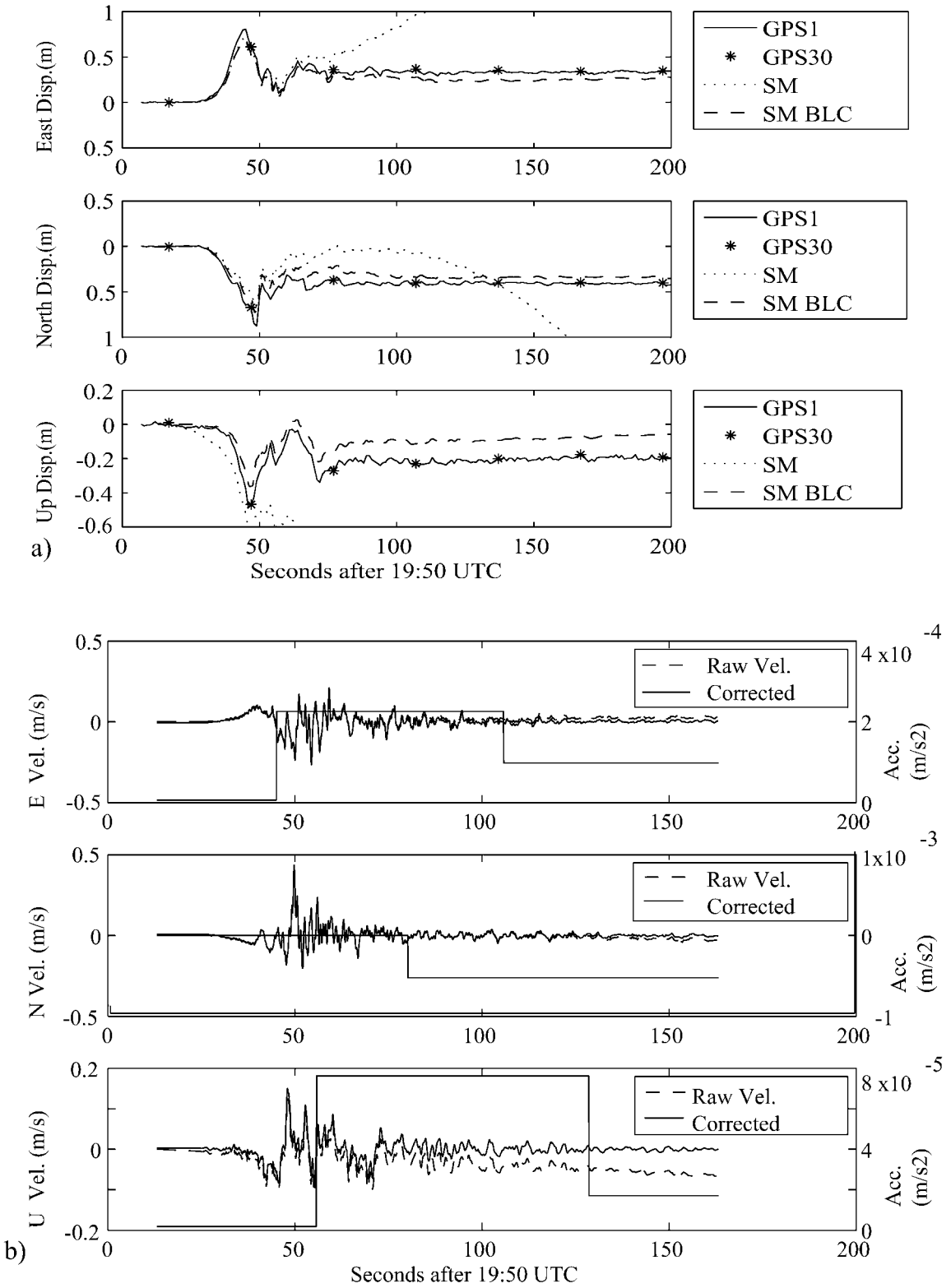

Figure 6. (a) Displacement constrained by a combination of GPS and strong-motion data is shown for GPS site 950120 and Knet site HKD138 (solid line, SM + GPS). The integrated uncorrected strong-motion data (dashed, SM) have large errors. (b) Velocity seismograms for the same site pairs.

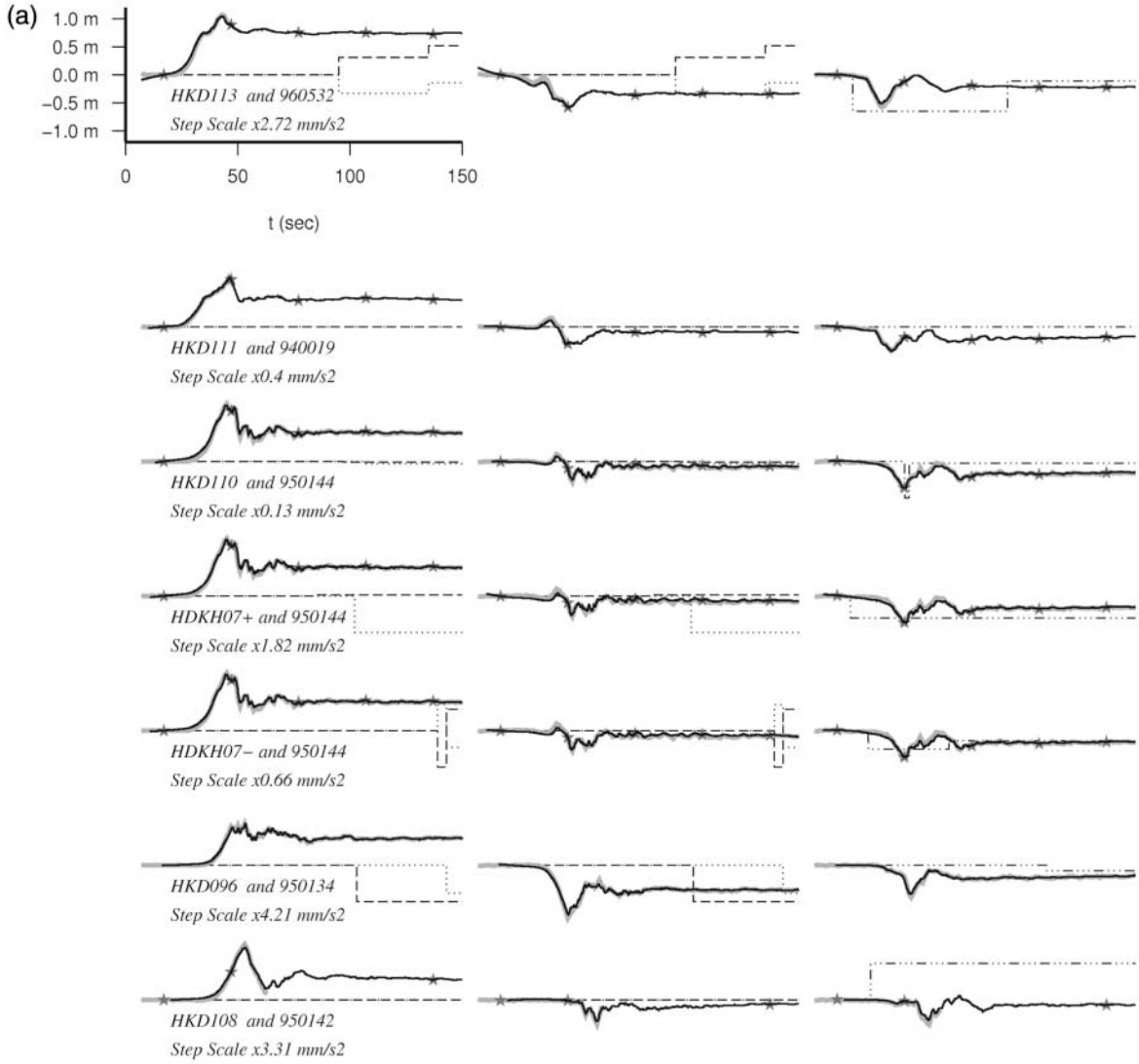

Figure 7. (a) Constrained displacement seismograms (dark line, SM + GPS) for sites 0 km to 155 km from the hypocenter, in order of increasing distance. 1-Hz GPS (gray line) and 30-sec GPS (stars) are also shown. Displacement is in meters using the same scale for all seismograms on the panel. The timing of the step function offsets is shown with the thin black lines, scaled by the amount indicated by the text in millimeters per second squared. Components are east, north, and up for the seismometers, while the step functions are left in the original sensor orientations described in Table 2. Both horizontal step function components have been plotted with the east and north components to clarify the relative timing of the rotated components. Surface Kiknet site names are indicated with a +. (*continued on next four pages*)

or two large steps with numerous small steps that are very poorly constrained, lending support to the approach of limiting the number of steps. The solutions with one or two steps then can be considered a test of the hypothesis that the data can be satisfied by using this simple model. Datasets that fail to retrieve a satisfactory solution indicate the possible presence of time-varying tilt.

Figure 7 shows the final solution for the combined GPS and seismic-displacement time series for each component of each site. Superimposed are the step function acceleration offset solutions for each component. A few features are particularly noticeable. First, the step function model for long-period offsets clearly appears to be valid for most cases, since the resulting high-frequency displacements match the 1-Hz GPS quite closely. In the sites examined, one or two steps were sufficient for the noise model. In addition, for 13 sites, the step functions appear to arise simultaneously on more than one component. Figure 9, in particular, demonstrates that the step functions found usually occurred well after the peak acceleration.

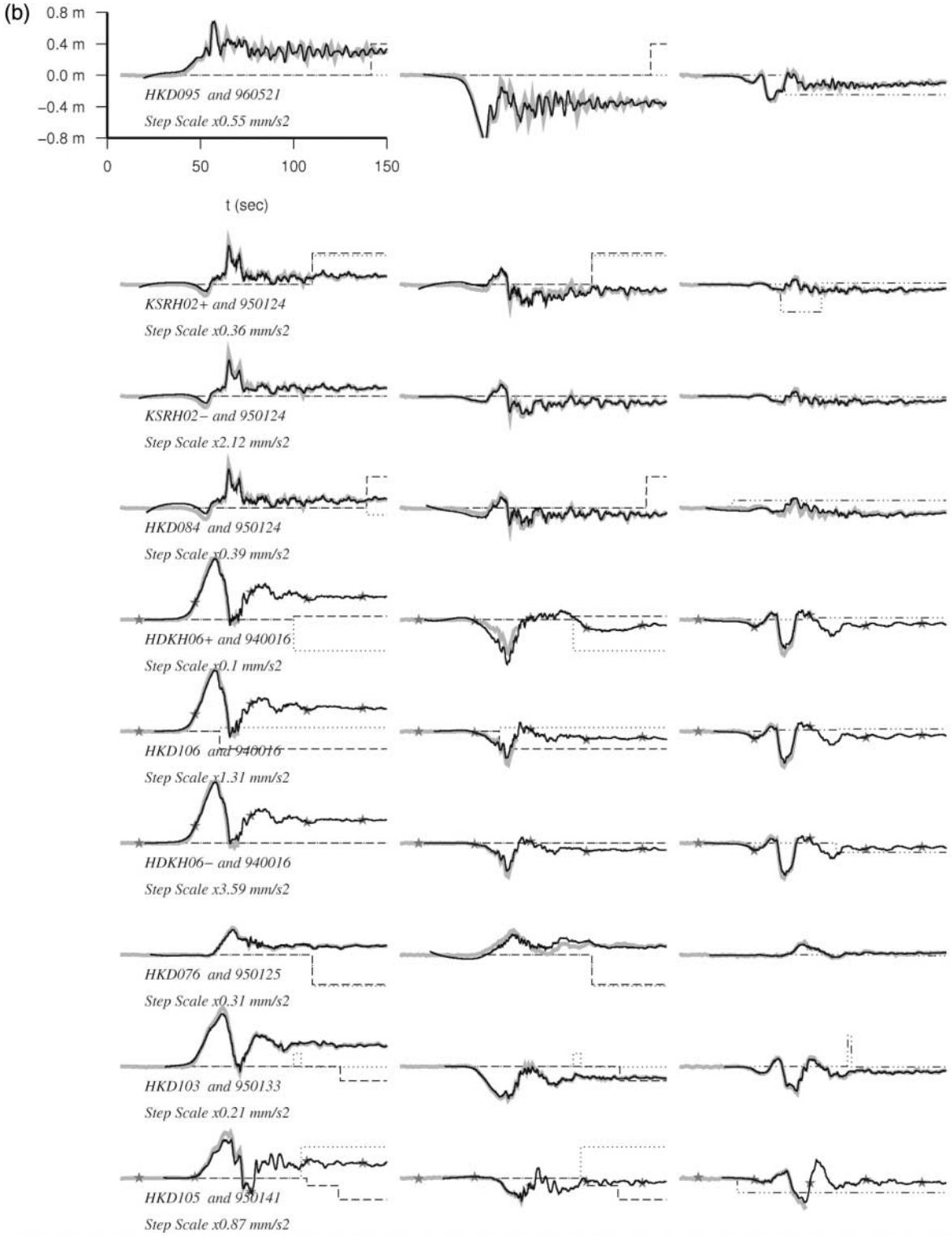

Figure 7. (*continued*) (b) Constrained displacement seismograms for sites 140 km to 200 km from the hypocenter. Plotting conventions are the same as for (a).

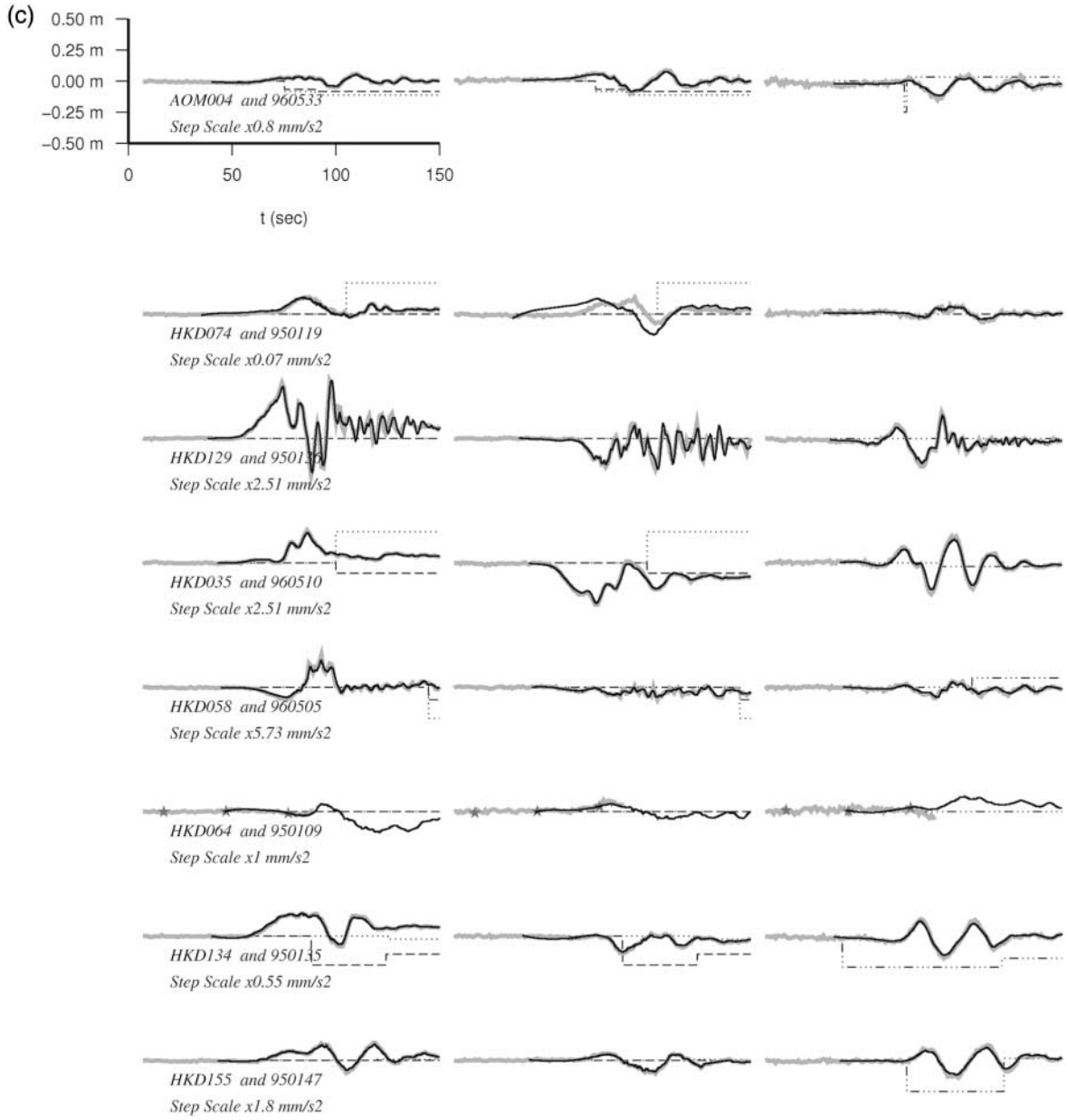

Figure 7. (*continued*) (c) Constrained displacement seismograms for sites 200 km to 275 km from the hypocenter. Plotting conventions are the same as for (a).

Comparison of Constrained Solution to Alternative Approaches

In all cases, the baseline-corrected displacement signal that was calculated without GPS as a constraint produced a time series with a postevent constant displacement. In some cases, the baseline-corrected (BLC) coseismic displacement even matched the GPS within the GPS margin for error. The differences between the BLC and GPS displacements are shown in Figure 11 as a function of distance from the epicenter. However, there was no reliable pattern among the 39 site pairs studied to predict which sites might recover a correct versus an incorrect baseline-corrected coseismic displacement. This is because, although a flat postevent displacement response is a necessary criterion for a baseline correction scheme, it may not reflect the true displacement (Boore and Bommer, 2005). This is shown well in Figures 10 and 11, where there are noticeable differences (easily up to 0.4 m) between the constrained and unconstrained coseismic deformations at the various strong-motion sites. Part of the problem with the baseline correction scheme is the lack of knowledge of the presence and number of step function offsets. When there can be more than one possible step within the active portion of the signal, such as with site HDK138 in Figure 6, it becomes a nontrivial task to decide how many

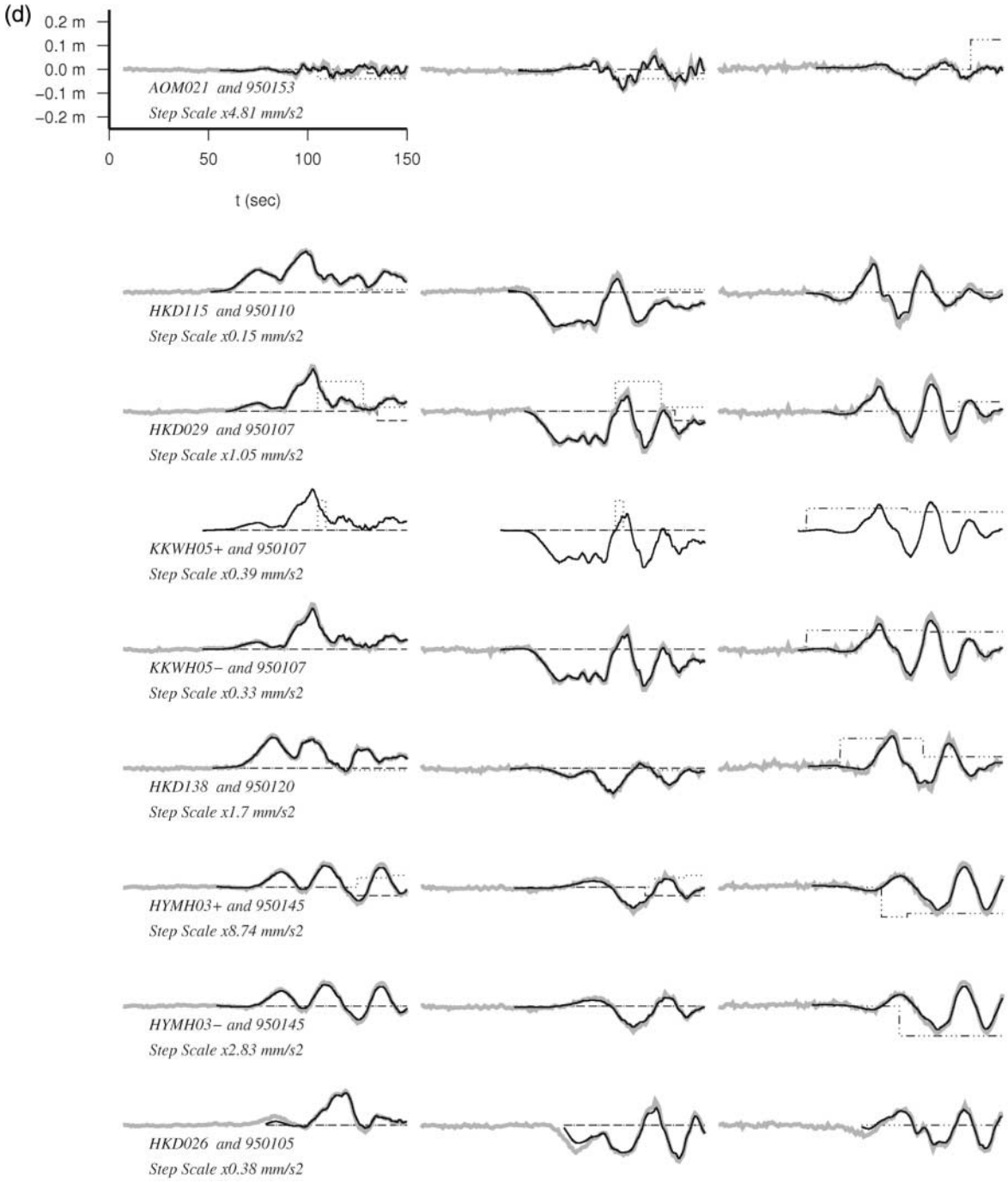

Figure 7. (*continued*) (d) Constrained displacement seismograms for sites 275 km to 360 km from the hypocenter. Plotting conventions are the same as for (a).

steps there should be and when they should take place, not to mention what their magnitude should be. Figure 11 shows that the differences between the 1-Hz GPS and the unconstrained baseline-corrected strong-motion coseismic displacements for the entire Hokkaido dataset tend to be larger at sites that are closer to the earthquake focus. A challenge with a traditional baseline correction scheme is the need for a well-defined pretrigger signal to establish an initial baseline. The GPS-constrained solution has no such requirement, and several useful displacement signals were retrieved when the initial *p* wave was not captured by the accelerometers at distant sites. For the BLC signals, the magnitude of the resulting static displacement is highly sensitive to the precise timing of the offset. If the coseismic offset is in disagreement with the GPS, the timing of the baseline correction offsets are likely to be in error. We therefore hesitate to draw further conclusions from these baseline correction errors.

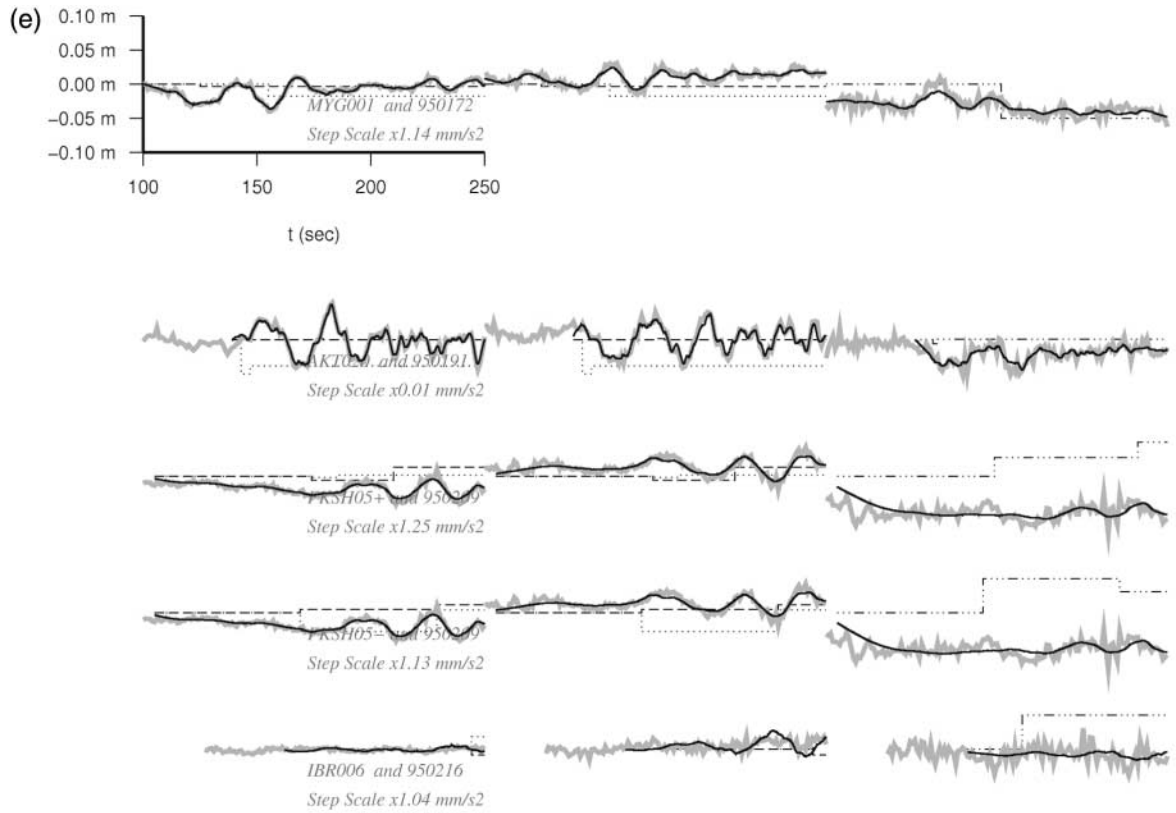

Figure 7. (*continued*) (e) Constrained displacement seismograms for sites 360 km to 700 km from the hypocenter. Plotting conventions are the same as for (a).

For comparative purposes, an error estimate for each component of the retrieved optimal displacements was computed that is consistent with the normalized standard deviation error used previously in the examination of site orientations. In this case, instead of using the difference between filtered displacement signals, the residual between the constrained solution and the unconstrained, rotated strong-motion signal modified by the noise model solution is used. This is described as

$$Err = \frac{\sum_{i=1}^{nt} \left(\left[\int_0^{t_i} \int_0^{t_i} (a_{\mathrm{SM}} - a_{\mathrm{step}}) dt^2 \right] - u_{\mathrm{GPS}i} \right)}{(nt - 1) \cdot \max(u_{\mathrm{GPS}i})} \quad (9)$$

in which a_{SM} are the unfiltered rotated strong-motion accelerations, a_{step} is the solved step function noise model, and $u_{\mathrm{GPS}i,j}$ are the 1-Hz GPS displacements (resampled at 10 Hz) for component j, and nt is the number of time samples. Once again, the strong-motion time series was shifted in time by an amount proportional to the difference in epicentral distance.

It was expected that the constrained, unfiltered solutions would tend to have higher errors computed than the filtered comparisons and, in general, this was the case. In multiple cases, however, the constrained signal was recovered with an error of the same order of magnitude as the filtered comparisons. For a few cases, the constrained solution was superior, by this metric. A few sites have an unusually large error associated with a single component. This is likely a sign that the step noise model assumption (involving only one or two steps) is insufficient to model the long-period behavior of that particular component.

With a set of step function models available, it is possible to gain some insight into potential causes of the errors. If it is assumed that these baseline steps were due to physical tilt of the sensor, the angle of tilt could be found from the steps in the horizontal components, as discussed earlier. In Figure 12, the assumed tilt is shown with respect to the range to the epicenter, and the corresponding acceleration is shown on the same scale. Larger offsets tend to occur for sites less than 200 km from the earthquake. However, there is no correlation between the size of the step function and the peak ground acceleration (Fig. 12b). Note that these assumed tilt angles are not related to the horizontal sensor misorientations discussed earlier. The tilts are much larger than would be expected from the tectonic tilt of the crust after the earthquake.

The timing of these steps is examined in Figure 13. The steps in the two horizontal components have a tendency to occur at the same time, and often about 50 sec after the *S*-wave arrival, whereas those in the vertical components

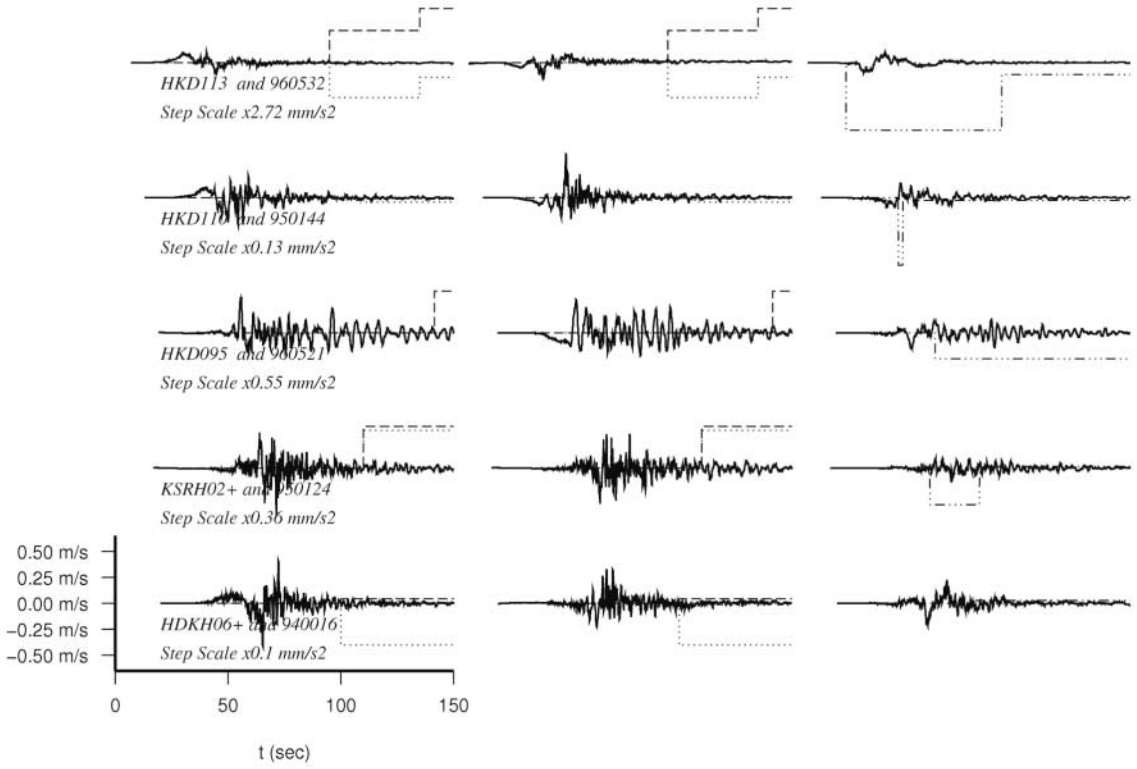

Figure 8. Constrained velocity seismograms for selected sites 0 km to 155 km from the hypocenter. Velocity is in meters per second using the same scale for all seismograms on the panel. The timing of the step function offsets is shown with the thin black lines, scaled by the amount indicated by the text in millimeters per second squared. Components are local sensor east, north, and up. Surface Kiknet site names are indicated with a +. Ⓔ The full set of sites may be found in the electronic edition of BSSA.

tend to lead the horizontal components. It could be argued that the steps in the horizontal components follow the arrival of the *S* wave, but the vertical components follow the arrival of the *P* wave. There is no systematic trend with distance, however, to indicate it is due to the higher amplitude shaking of a particular seismic phase. Though the data are not a Gaussian distribution, a fit to the timing of the steps reproduces a trend close to the *P*-wave velocity. This may indicate a possible relation to the triggering algorithm or changes related to the gain of the instrumentation.

This work was done using 1-Hz GPS data as a constraint the strong-motion records. This limits the set of strong-motion sites that can use this approach to those with a permanent 1-Hz GPS station within a radius of approximately 15 km for this size event, according to Figure 4c. However, during the 2003 Tokachi-Oki event, the communications link to GEONET site 940016 went down and made 1-Hz data unavailable after 70 sec, during the most active portion of the signal, but the buffered 30-sec data were recovered. It appeared that if the 30-sec data are used as an additional constraint, the entire length of the time series could be successfully processed. This supposition was tested using data for the site pair GEONET 950144 and Knet HKD110, which had 1-Hz and 30-sec GPS for the entire duration. As Figure 14 shows, the results from the use of a 30-sec constraint alone compare well to the fully constrained solution. This would be of most benefit for large events where there are a few 30-sec samples within the major period of strong ground motion, and where the coseismic offsets are greater than the error level of the GPS estimates. However, 30-sec GPS data are not sufficient for resolving misorientations of the sensors.

Conclusions

Traditional techniques for recovering a coseismic static offset by making a baseline correction to velocity seismograms to account for one- or two-step functions in acceleration were found to be adequate for only a few cases. The comparison of integrated strong-motion records with 1-Hz GPS displacement records indicates that only 5% of the time does the static displacement retrieved from baseline correction processing agree with the actual displacement to within 9%. This 9% quantity is approximately the assumed accuracy of the ground motions used in source inversions (e.g., Miyazaki *et al.*, 2004a, 2004b).

Using a constrained inversion technique, the optimal displacement records were found that satisfy the 1-Hz GPS

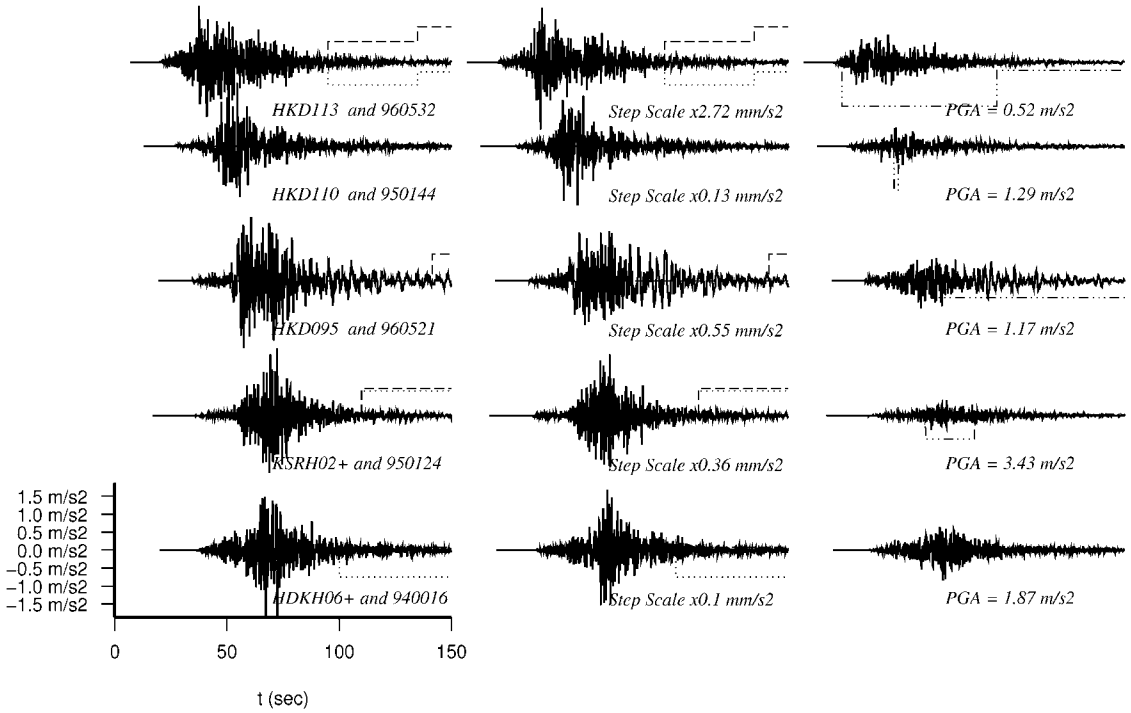

Figure 9. Constrained acceleration records for selected sites 0 to 155 km from the hypocenter. Acceleration is in meters per second squared. The timing of the step function offsets is shown with the thin black lines, scaled by the amount indicated by the text in millimeters per second squared. Components are east, north, and up. Surface Kiknet site names are indicated with a +. Records for each site are normalized to the peak ground acceleration. Ⓔ The full set of sites may be found in the electronic edition of BSSA.

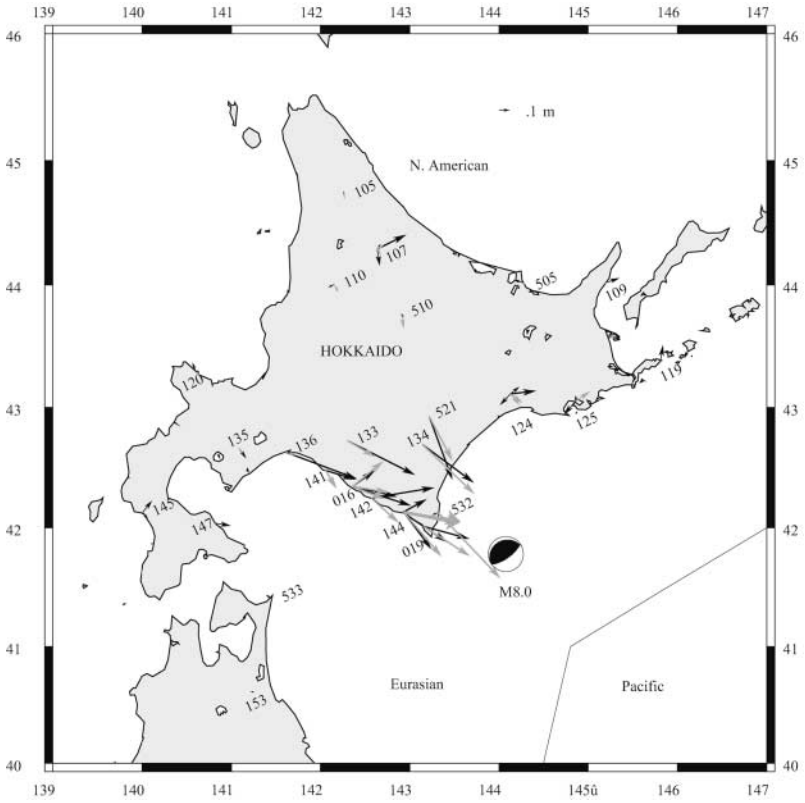

Figure 10. Coseismic displacement from 1-Hz GPS (gray arrows) and from baseline-corrected strong-motion seismograms (black arrows). Large errors in the coseismic displacement estimated from the baseline-corrected data tend to occur closer to the epicenter and are comparable in size to the total displacement.

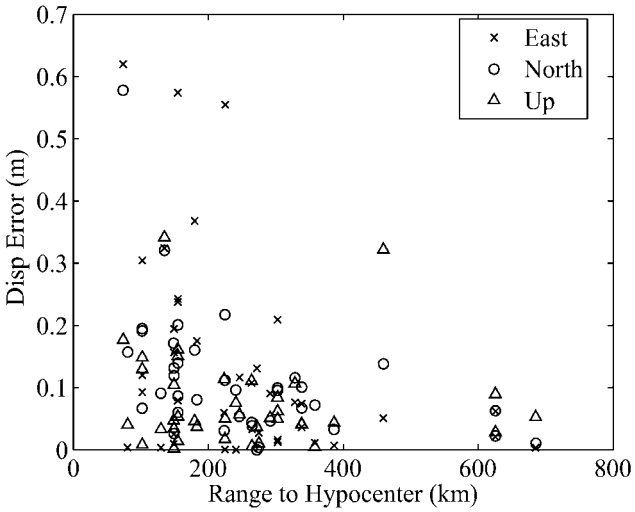

Figure 11. Coseismic displacement error calculated as the difference between the 1-Hz GPS static displacement and the baseline-corrected coseismic displacement, plotted as a function of distance. Larger errors tend to occur at shorter distances where ground motions are bigger.

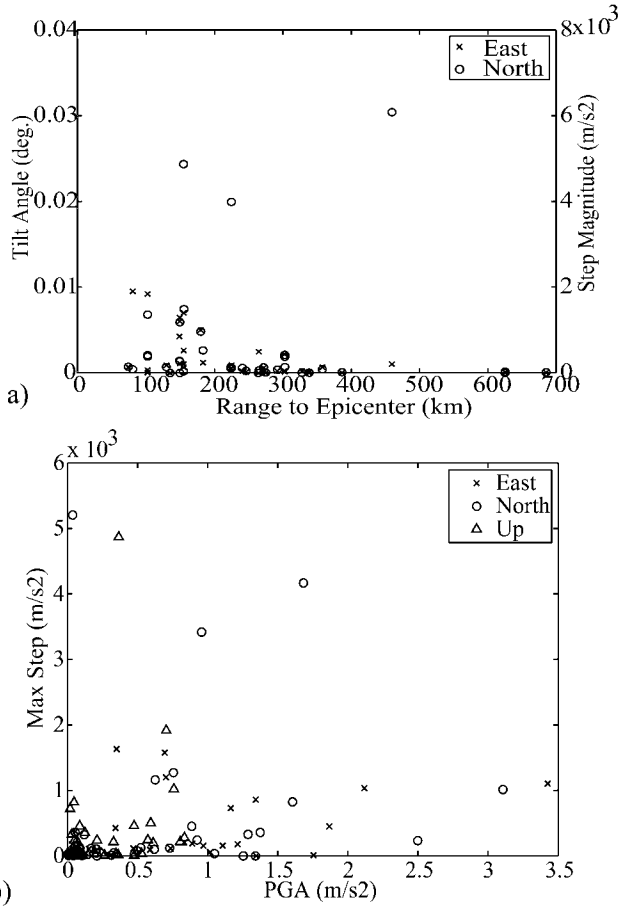

Figure 12. (a) Tilt angles for each horizontal sensor component as a function of distance to the epicenter. This assumes that the step function in acceleration is due to physical tilting of the instrument. Right-hand scale is the equivalent acceleration step offset size. (b) Magnitudes of the step functions compared with the peak ground acceleration (PGA) at the same sites. The step magnitudes do not appear to be strongly correlated with the PGA.

data and the seismic data while simultaneously solving for a single step function offset, or maximum two-step offsets, in the acceleration record. The acceptable level of misfit is determined by comparing the high-pass-filtered signals. In 44 of 117 channels or 38% of all channels examined, one step function in acceleration decreases the misfit to an acceptable misfit level. In 14 channels (12% of all channels), two-step functions are sufficient to decrease the misfit to an acceptable misfit level. All but six of the remaining channels had a clear minimum in the misfit with one- or two-step functions that justified the use of this model.

The step function noise in the acceleration could be caused by an instantaneous tilt of the instruments, for example, due to local ground failure or to shifting of the instrument base, which in most cases would be on the order of 10^{-3} deg, but for a few cases would be as much as 0.037 deg. Tectonic tilt due the changed geometry of the plates after the subduction earthquake is on the order of 10^{-4} deg, and is therefore too small to be the cause. This would imply that these are local ground-deformation effects. This is a potential explanation at seven sites, where the step functions occur very close in time on the two horizontal components, implying that an instantaneous tilt could be the source. However, we have shown that for most of the sites (80%), the time of the acceleration offset on the horizontal components is usually after the strongest shaking has ended. Therefore, it could be due to artifacts in the electronics of the instrument; for example a small gain change linked to the triggering algorithm, which may be consistent with the slight tendency of the offsets to occur often about 75 sec after the start time of the recording triggered by the *P* wave.

The six channels where it is not possible to satisfy both datasets with one or two steps may be an indication of instrumental drift or significant time-varying tilt of the seismic instrument that was occurring throughout the period of shaking. The magnitude of temporal rotational motions in seismometers due to strong ground motion can be much larger than the static seismic tilts (Castellani and Zembati, 1994; Igel *et al.*, 2005). Such motion might be expected where there is amplification in sedimentary basins; however, only one site pair is notably located in a large basin (GEONET 950133 and Knet HKD129), and this site does not exhibit any large steps in the first 200 sec. Another option is an instrument baseline shift due to hysteresis during an episode of strong shaking (Irwan *et al.*, 1985). Local ground failure cannot be excluded for at least 36 sites where average shear-wave velocity (V_S) in the top 10 meters of less than 350 m/sec indicate that they cannot be considered firm rock sites. We found no correlation between V_S in the top 10 meters and the magnitude of the tilt, however.

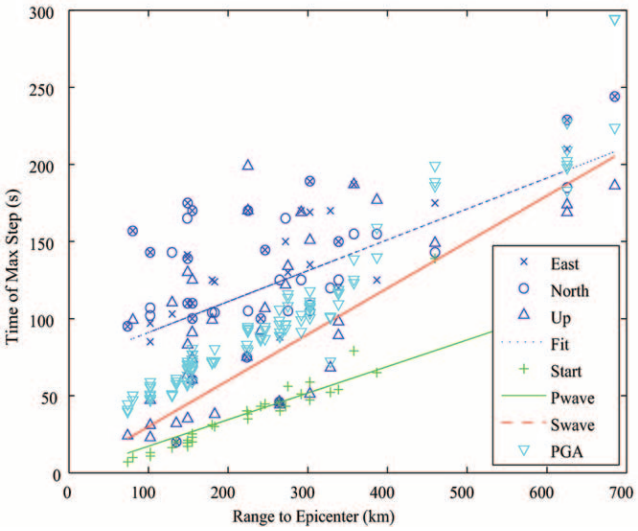

Figure 13. Time of the largest solved step offsets (×, ○, Δ) as a function of epicentral distance for east (×), north (○), and up (Δ) components. Many sites show step functions that are coincident in time on both of the horizontal components, indicating possible tilting of the seismometer. + indicates the start time of the recording and ∇ indicates the time when the peak ground acceleration (PGA) was recorded. A *P*-wave velocity of 5.8 m/sec is indicated by the green solid line, and *S*-wave velocity of 3.3 m/sec is indicated by the red line. The trigger times of the records are based on the *P*-wave arrival, and the maximum accelerations usually occur about 20 sec after the predicted *S*-wave arrival. A fit to the times of the step offsets for all three components is nearly parallel to the *P*-wave velocity. Only the vertical components contain steps before the arrival of the *S* wave. In fact, most of the offsets in the horizontal components occur long after the strongest shaking.

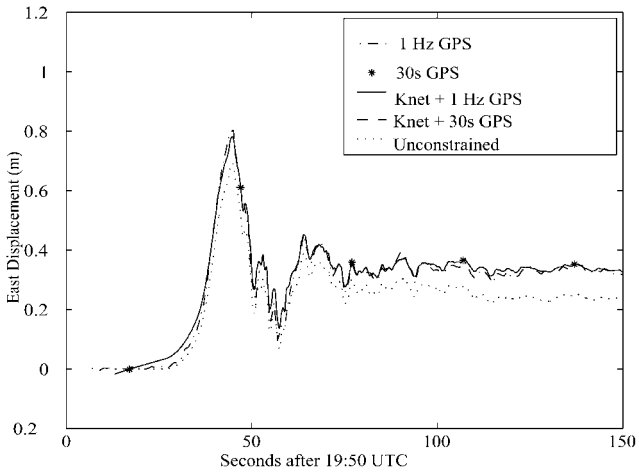

Figure 14. Constrained displacement solutions for GEONET 950144 and Knet HKD110 using the full 1-Hz GPS constraint (solid line, Knet + 1 Hz GPS), and 30-sec GPS constraint only (dashed line, Knet + 30s GPS). The original 1-Hz GPS time series is shown as a dot-dashed line, and the 30-sec GPS is shown by stars. The solution using only the 30-sec GPS as a constraint is almost identical with the result using the 1-Hz GPS for an event of this magnitude. Some differences are evident in the early part of the record, which may be due to the relatively short pretrigger time series. A baseline-corrected strong-motion signal is also shown for comparison as a dotted line.

At five sites, large step functions occurred very close in time on all three components. If we assumed a tilt that could produce the observed offsets on the horizontal components, the observed vertical component is much too large to be explained as the corresponding vertical tilt effect; therefore, it is more likely to be a problem in the electronics that is common to all channels, or other nonlinear response of the sensor. At one site, a step on one horizontal component occurred at the same time as a step on the vertical component, with the same likely cause.

In many cases the step functions occurred on the three components at different times, leading to a conclusion that a change or drift may have occurred on the individual sensor electronics. Finally, at 7 of the 39 sites, no correction was needed on any of the three components for the first 150 sec of the signal.

There is a some evidence that the step functions can be larger at sites closer to the epicenter, which is the only support found for a correlation with amplitude of shaking at a site. No correlation was found between the time or size of the step functions and the time or magnitude of the peak ground acceleration. Of the six borehole KiKnet sites examined, four exhibited similar step timing between the uphole and downhole records on at least one component. This is surprising because one would expect borehole installations to be less susceptible to effects such as tilt due to local ground failure, and would be prompted to look for a common source of noise in the electronics. In three of these four cases the magnitude of the step functions was smaller for the downhole component.

Large sensor misorientations were found at both Knet and Kiknet sites. Nine of 39 sites had misorientations greater than 20 deg. These orientations have been presented in Table 2.

We have demonstrated the potential for using these techniques for colocated strong-motion and 30-sec GPS sites. Results using 1-Hz and 30-sec GPS time series were compared and showed very good agreement. For an event the size of the Hokkaido event, where there is significant energy at frequencies of 20 sec and lower, the integration of the seismic waveforms is sufficiently constrained by the 30-sec GPS solutions. This extends the applicability for using the technique on many more sites where 30-sec GPS data are available. These 30-sec data, however, would not be sufficient for checking the sensor orientation.

Often, for source inversion studies, seismic data are used in conjunction with coseismic offsets determined from daily GPS solutions, essentially an average position for the GPS site using data recorded continuously over one day be-

fore comparing with the solution for one day after. This assumes that there was no change in site position over the daylong period. Using 1-Hz GPS allows one to distinguish better between coseismic and postseismic displacement, which can be important because of the potential for large postseismic changes within the first 24 hours after the event, as was the case for the Hokkaido earthquake (Miyazaki *et al.*, 2004b).

Acknowledgments

This work was made possible by the National Science Foundation under Grants 0337549 and 0337206, NEHRP Grant 20050036 to the University of Colorado, and a NASA Earth System Science Fellowship (for K.C.). We thank the National Research Institute for Earth Science and Disaster Prevention (NIED) and the Geographic Survey Institute (GSI) for access to the seismic and GPS data. We would also like to thank Andrea Bilich, Paul Bodin, Dave Boore, John Clinton, Joan Gomberg, Tom Heaton, Kojiro Irikura, Shin'ichi Miyazaki, and Dave Wald for helpful discussions.

References

Abrahamson, N. A., and W. Silva (1997). Empirical response spectral attenuation relations for shallow crustal earthquakes, *Seism. Res. Lett.* **68,** 94–127.

Altamimi, Z., P. Sillard, and C. Boucher (2002). ITRF2000: a new release of the International Terrestrial Reference Frame for Earth science applications, *J. Geophys. Res.* **107,** 2214.

Aoi, S., T. Kunugi, and H. Fujiwara (2004). Strong motion seismograph network operated by NIED: Knet and KiK-net, *J. Jpn. Assoc. Earthquake Eng.* **4,** 65–74.

Aoi, S., K. Obara, S. Hori, K. Kasahara, and Y. Okada (2000). New strong-motion observation network: Kik-net (abstract), *EOS Trans. AGU* **81,** no. 48 (Fall Meet. Suppl.), S71A-05.

Beutler, G., I. Mueller, and R. Neilan (1994). The International GPS Service for Geodynamics (IGS): development and start of official service on January 1, 1994, *Bull. Geod.* **68,** 39–70.

Boore, D. (2001). Effect of baseline corrections on displacements response spectra for several recordings of the 1999 Chi-Chi, Taiwan, earthquake, *Bull. Seism. Soc. Am.* **91,** 1199–1211.

Boore, D. M., and J. J. Bommer (2005). Processing of strong-motion accelerograms: needs, options, and consequences, *Soil Dyn. Earthquake Eng.* **25,** 93–115.

Boore, D. M., C. D. Stephens, and W. B. Joyner (2002). Comments on baseline correction of digital strong-motion data: Examples from the 1999 Hector Mine, California, earthquake, *Bull. Seism. Soc. Am.* **92,** 1543–1560.

Boore, D. M., W. B. Joyner, A. A. Oliver III, and R. A. Page (1980). Peak acceleration, velocity, and displacement from strong-motion records, *Bull. Seism. Soc. Am.* **70,** 305–321.

Castellani, A., and Z. Zembaty (1994). Stochastic modeling of seismic surface rotations, *Nat. Hazards* **10,** 181–191.

Celebi, M. (2000). GPS in dynamic monitoring of long-period structures, *Soil Dyn. Earthquake Eng.* **20,** 477–483.

Clinton, J. F. (2004). Modern digital seismology—instrumentation, and small amplitude studies in the engineering world, Ph.D. Thesis, California Institute of Technology.

Converse, A. M., and A. G. Brady (1992). BAP: basic strong-motion accelerogram processing software; Version 1.0, *U.S. Geol. Surv. Open-File Rept. 92-296A*, 178 pp,

Darragh, B., W. Silva, and N. Gregor (2004). Strong motion record processing for the PEER Center, Presented at Invited Workshop on Strong Motion Record Processing, 26–27 May 2004, Consortium of Organizations for Strong-Motion Observation Systems (COSMOS), Richmond, California.

Graizer, V. M. (2004). Record processing considerations for the effects of tilting and transients, Presented at Invited Workshop on Strong Motion Record Processing, 26–27 May 2004, COSMOS, Richmond, California.

Hartzell, S. H., and T. H. Heaton (1983). Inversion of strong ground motion and teleseismic waveform data for the fault rupture history of the 1979 Imperial-Valley, California, earthquake, *Bull. Seism. Soc. Am.* **73,** 1553–1583.

Honda, R., S. Aoi, N. Morikawa, H. Sekiguchi, T. Knugi, and H. Fujiwara (2004). Ground motion and rupture process of the 2003 Tokachi-oki earthquake obtained from strong motion data of K-net and KiK-net, *Earth Planets Space* **56,** 317–322.

Igel, H., U. Schreiber, A. Flaws, B. Schuberth, A. Velikoseltsev, and A. Cochard (2005). Rotational motions induced by the M8.1 Tokachi-oki earthquake, Sept. 25, 2003, *Geophys. Res. Lett.* **32,** L08309.

Irwan, M., F. Kimata, K. Hirahara, T. Sagiya, and A. Yamagiwa (2004). Measuring ground deformations with 1-Hz GPS data: the 2003 Tokachi-oki earthquake (preliminary report), *Earth Planets Space* **56,** 389–393.

Irwan, W. D., M. A. Moser, and C.-Y. Peng (1985). Some observations on strong-motion earthquake measurement using a digital accelerograph, *Bull. Seism. Soc. Am.* **75,** 1225–1246.

Ji, C., K. M. Larson, Y. Tan, K. W. Hudnut, and K. Choi (2004). Slip history of the 2003 San Simeon earthquake constrained by combining 1-Hz GPS, strong motion, and teleseismic data, *Geophys. Res. Lett.* **31,** L17608.

Kinoshita, S. (1998). Kyoshin net (k-net), *Seism. Res. Lett.* **69,** 309–332.

Koketsu, K., K. Hikima, S. Miyazaki, and S. Ide (2003). Joint inversion of strong motion and geodetic data for the source process of the 2003 Tokachi-oki, Hokkaido, earthquake, *Earth Planets Space* **55,** 1–6.

Larson, K. M., P. Bodin, and J. Gomberg (2003). Using 1-Hz GPS data to measure deformations caused by the Denali fault earthquake, *Science* **300,** 1421–1424.

Lichten, S. M., and J. S. Border (1987). Strategies for high-precision global positioning system orbit determination, *J. Geophys. Res.* **92,** 12,751–12,762.

Loh, C.-H. (2004). Strong motion data processing in Taiwan and its engineering application, Presented at Invited Workshop on Strong-motion Record Processing, 26–27 May 2004, Consortium of Organizations for Strong-Motion Observation Systems (COSMOS), Richmond, California.

Miura, S., Y. Suwa, A. Hasegawa, and T. Nishimura (2004). The 2003 M8.0 Tokachi-Oki earthquake: how much has the great event paid back slip debts? *Geophys. Res. Lett.* **31,** L05613.

Miyazaki, S., K. M. Larson, K. Choi, K. Hikima, K. Kotetsu, P. Bodin, J. Haase, G. Emore, and A. Yamagiwa (2004a). Modeling the rupture process of the 2003 September 25 Tokachi-Oki (Hokkaido) earthquake using 1-Hz GPS data, *Geophys. Res. Lett.* **31,** L21603.

Miyazaki, S., T. Saito, M. Sasaki, S. Hatanaka, and Y. Iimura (1997). Expansion of GSI's nationwide GPS array, *Bull. Geograph. Surv. Inst.* **43,** 23–34.

Miyazaki, S., P. Segall, J. Fukuda, and T. Kato (2004b). Space time distribution of afterslip following the 2003 Tokachi-oki earthquake: implications for variations in fault zone frictional properties, *Geophys. Res. Lett.* **31,** L06623.

Okada, Y. (1985), Surface deformation due to shear and tensile faults in a half-space, *Bull. Seism. Soc. Am.* **75,** 1135–1154.

Okada, Y., K. Kasahara, S. Hori, K. Obara, S. Sekiguchi, H. Fujiwara, and A. Yamamoto (2004). Recent progress of seismic observation networks in Japan—Hi-net, F-net, K-NET and KiK-net, *Earth Planets Space* **56,** 15–28.

Segall, P., and J. L. Davis (1997). GPS applications for geodynamics and earthquake studies, *Ann. Rev. Earth Planet. Sci.* **25,** 301–336.

Shakal, A., V. Graizer, M. Huang, R. Borcherdt, H. Haddadi, K. Lin, C. Stephens, and P. Roffers (2005). Preliminary analysis of strong-

motion recordings from the 28 September 2004 Parkfield, California, Earthquake, *Seism. Res. Lett.* **76,** 27–39.

Shakal, A. F., M. Huang, and V. Graizer (2004). CSMIP strong-motion data processing, Presented at Invited Workshop on Strong-Motion Record Processing, 26–27 May 2004, Consortium of Organizations for Strong-Motion Observation Systems (COSMOS), Richmond, California.

Spencer, B. F., E. Johnson, and J. Ramallo (2000). "Smart" isolation for seismic control, *JSME Int. J. Ser. C* **43,** 704–711.

Stephens, C. D., and D. M. Boore (2004). ANSS/NSMP strong-motion record processing and procedures, Presented at Invited Workshop on Strong-Motion Record Processing, 26–27 May 2004, Consortium of Organizations for Strong-Motion Observation Systems (COSMOS), Richmond, California.

Symans, M. D., G. J. Madden, and N. Wongprasert (1999). Semi-active hybrid isolation systems: addressing the limitations of passive isolation systems, in *Proc. of Structures Congress*, ASCE, New Orleans, Louisiana, 862–865.

Trifunac, M. D. (1977). Uniformly processed strong motion earthquake ground accelerations in the western United States of America for the period from 1933 to 1971: pseudo relative spectra and processing noise, Report CE 77-044, University of Southern California, Los Angeles, California.

Trifunac, M. D., and V. Lee (1978). Uniformly processed strong earthquake ground accelerations in the western United States of America for the period from 1933 to 1971: corrected acceleration, velocity and displacement curves, Report CE 78-01, Department of Civil Engineering, University of Southern California, Los Angeles, California.

Trifunac, M. D., and M. I. Todorovska (2001). A note on the usuable dynamic range of accelerographs recording translation, *Soil Dyn. Earthquake Eng.* **21,** 275–286.

Wald, D. J., and T. H. Heaton (1994). Spatial and temporal distribution of slip for the 1992 Landers, California, earthquake, *Bull. Seism. Soc. Am.* **84,** 668–691.

Yagi, Y. (2004). Source rupture process of the 2003 Tokachi-oki earthquake determined by joint inversion of teleseismic body wave and strong ground motion data, *Earth Planets Space* **56,** 311–316.

Yamagiwa, A., Y. Hatanaka, T. Yutsudo, and B. Miyahara (2006). Real time capability of GEONET system and its application to crust monitoring, *Bull. Geograph. Surv. Inst.* **55,** 27.

Yamanaka, Y., and M. Kikuchi (2003). Source process of the recurrent Tokachi-oki earthquake on September 26, 2003, inferred from teleseismic body waves, *Earth Planets Space* **55,** E21–E24.

Department of Earth & Atmospheric Sciences
550 Stadium Mall Drive
Purdue University
West Lafayette, Indiana 47907-2051
gemore@purdue.edu
(G.L.E., J.S.H.)

Department of Aerospace Engineering Sciences
UCB 429
University of Colorado
Boulder, Colorado 80309-0429
(K.C., K.M.L.)

Geodetic Observation Center
Geographical Survey Institute (GSI)
Kitasato 1, Tsukuba city, Ibaraki pref., 305-0821
Japan
(A.Y.)

Manuscript received 7 July 2006.